Reflection and Transmission of Plane Elastic Waves at an Interface Between Two Double-Porosity Media: Effect of Local Fluid Flow

Enjiang Wang[1] · José M. Carcione[1,2] · Jing Ba[1] · Yang Liu[3]

Abstract

We obtain the reflection and transmission coefficients for inhomogeneous plane waves incident on a flat interface separating two double-porosity media described by the Biot–Rayleigh model, which takes into account the effect of local fluid flow (LFF). Three longitudinal and one transverse waves are reflected and transmitted, represented by potential functions specified by the propagation and attenuation directions. The continuity of the energy at the interface for sealed and open-boundary conditions yields a system of equations for the coefficients, and the expressions of the energy ratios for the reflected and refracted waves are derived in closed form. Numerical examples showing the magnitude, phase and energy ratio as a function of frequency and incidence angle are carried out to investigate the influence of the inhomogeneity angle, boundary condition, type of incidence wave and LFF effect. The results confirm that the LFF affects the reflection and transmission behaviors for the incident P1 and SV waves, irrespective of whether the interface is open or sealed. The effect causes interference fluxes between different waves, a consequence of energy conservation at the interface. We also perform full-waveform simulations to validate the results.

Keywords Double-porosity medium · Reflection and transmission coefficients · Local fluid flow (LFF) · Energy partition · Inhomogeneous plane wave

✉ Jing Ba
jba@hhu.edu.cn

[1] School of Earth Sciences and Engineering, Hohai University, Nanjing 211100, China

[2] Istituto Nazionale di Oceanografia e di Geofisica Sperimentale (OGS), Borgo Grotta Gigante 42c, 34010 Sgonico, Trieste, Italy

[3] State Key Laboratory of Petroleum Resources and Prospecting, China University of Petroleum, Beijing 102249, China

 Springer

1 Introduction

The study of wave reflection and transmission at an interface separating two fluid-saturated porous media is of interest in a variety of fields, such as geomechanics, hydrogeology, petroleum engineering, soil dynamics, and exploration geophysics (Deresiewicz and Rice 1962; Cui and Wang 2003; Tomar and Arora 2006; Dai et al. 2006a; Yeh et al. 2010; Sharma 2013; Carcione 2014). A better understanding of it is crucial for quantitatively inferring spatial distributions of key medium properties, such as permeability and porosity.

Various theories have been presented to describe wave motion in porous rocks. Biot (1956, 1962) pioneered the study and derived fundamental constitutive relations for analyzing wave motion in a medium saturated by a single viscous fluid. The theory predicts the existence of two compressional waves and one shear wave. Based on it, Deresiewicz and Rice (1962, 1964) studied the reflection and transmission coefficients at normal incidence. Extensions to more general cases of oblique incidence were carried out by Dutta and Odé (1983). The reflection and transmission at a plane interface between a fluid and a Biot medium were also studied (Santos et al. 1992), and more work was performed by Denneman et al. (2002) and Gurevich et al. (2004). The related boundary conditions have been applied to full-waveform modeling in complex environments by Sidler et al. (2013) among others.

Biot's theory describes wave propagation in media saturated with a single fluid. Brutsaert (1964) introduced extended Biot's theory to the case of immiscible fluids, and Santos et al. (1990) presented a similar model by considering two fluids and surface tension. These theories predict the existence of an additional highly attenuated compressional wave, due to the capillary pressure. A comprehensive study on wave motion in porous solids saturated with multiphase fluids was also given in Tuncay and Corapcioglu (1997). Based on this theory, the reflection and transmission characteristics at an interface between an elastic medium and a porous solid saturated by two immiscible fluids were investigated (Tomar and Arora 2006; Sharma and Kumar 2011). However, a main drawback of these approaches is that they neglect inertial coupling effects. Lo et al. (2005) considered the inertial effect, as well as other researchers (Arora and Tomar 2008; Yeh et al. 2010; Kumar and Saini 2012; Kumar and Sharma 2013; Shekhar and Parvez 2016). The influences of pore fluid, frequency, pore connections and wave inhomogeneity on the amplitude and energy of the reflected and transmitted waves were comprehensively investigated in Kumar and Sharma (2013).

Studies considering more than one solid (two frames) have also been performed. Leclaire et al. (1994) presented a Biot-type three-phase theory based on first principles, where the solid frame, ice particles and unfrozen water coexist. The theory assumes no interaction between the solids and predicts the existence of three compressional waves and two shear waves. The interaction between the mineral and ice particles was further included by Carcione and Tinivella (2000), and the theory was used to obtain the reflection coefficients related to a bottom simulating reflector. A more rigorous generalization to the case of non-uniform porosity for media with composite solids saturated by a single fluid was given in Carcione and Seriani (2001) and Santos et al. (2004). Using this theory, Rubino et al. (2006) studied the behavior of the energy reflection and transmission coefficients at an interface separating two porous media. Arora et al. (2015) further presented a four-phase poroelastic theory, in which the medium is composed of two solids and saturated by two fluids. The theory considers the interference fluxes and

predicts the coexistence of four compressional waves and two shear waves. Following this theory, Painuly and Arora (2018) studied the reflection and transmission of inhomogeneous waves.

Apart from the aforementioned theories, other researchers extended Biot's poroelastic theory to the case of double-porosity. Berryman and Wang (2000) presented a double-porosity/dual-permeability model, such that storage porosity and fracture porosity are both considered. Based on this theory, Dai et al. (2006a, b) studied the reflection and transmission at the interface between an elastic solid and a double-porosity medium, as well as between a fluid-saturated porous solid and a double-porosity medium. The effects of frequency, incidence angle, fracture permeability, porosity, and boundary conditions were studied. This theory was further improved by Pride and Berryman (2003a, b), in which a frequency-dependent compressibility law describes macroscopic fluid transfer between the porous constituents. The improved theory models realistic attenuation levels due to wave-induced fluid flow. It reduces to the effective Biot theory if the heterogeneity phase is assumed to be embedded in the host phase (Pride et al. 2004). Based on this effective theory, Zhao et al. (2015) investigated the effects of wave-induced fluid flow on wave signatures of seismic reflectivity.

Wave propagation in heterogeneous porous media induces fluid pressure gradients and consequently local fluid flow (LFF). LFF causes viscous loss and leads to energy dissipation at a mesoscopic scale, which is responsible for intrinsic wave attenuation at seismic frequencies (Pride et al. 2004; Müller et al. 2010). Over the past decades, significant efforts have been made to understand the mesoscopic loss mechanism due to LFF (Gurevich et al. 1997; Pride and Berryman 2003a; Carcione and Picotti 2006; Brajanovski et al. 2006; Agersborg et al. 2009; Müller et al. 2010; Carcione et al. 2010; Ba et al. 2011). Among these, the double-porosity model is notably a simple and effective one. Apart from Pride and Berryman's theory, Ba et al. (2011) derived another set of equations for describing wave propagation in double-porosity media based on Biot's theory of poroelasticity and Rayleigh model of bubble oscillations. The governing equations associated with LFF are described by a generalization of Rayleigh's theory of liquid collapse of a spherical cavity. Numerical examples show that this theory explains the levels of dispersion and attenuation in the seismic frequency band and predicts the existence of an additional highly attenuated compressional wave. Using this theory, Sharma (2013) studied the effect of LFF on the reflected waves but considered only the free surface of a double-porosity medium. Until now, the reflection and transmission problems between fluid-saturated double-porosity media, that take into account the LFF, have not been investigated.

The wave-induced LLF affects wave propagation and hence affects the behavior of the reflection and transmission coefficients, particularly in double-porosity media. The present work aims at investigating the influence of LFF on the reflection and transmission behaviors at an interface between two double-porosity media. For an oblique incidence (P1 wave or SV wave) upon the interface, three compressional and one transverse waves are reflected and transmitted. The waves are described by potential functions depending on the propagation and attenuation directions and the complex velocity. The particle displacements, solid stresses and fluid pressures are derived from these potentials by using the non-uniform porosity constitutive relations. The expressions for the reflection and transmission coefficients, as well as the corresponding energy ratios, are derived in closed form for open and sealed boundaries. The effects of the frequency and inhomogeneity angle are further discussed. Numerical wavefield simulations corresponding to the reflection and transmission problem are carried out to validate the results derived from the analysis.

2 Biot–Rayleigh Theory

The Biot–Rayleigh double-porosity medium (Ba et al. 2011) considers spherical inclusions embedded into an unbounded host medium, where two kinds of porosities and the same fluid coexist, namely a porosity ϕ_{10} of the host medium with a large volume fraction v_1, and a porosity ϕ_{20} of spherical inclusions with a lower volume fraction $v_2 = 1 - v_1$. The two porosities correspond to different permeabilities and compressibilities, and hence LFF is induced during wave propagation. The theory is based on the following assumptions: (1) the inclusions are spherical and homogeneous with a radius that is much smaller than the wavelength; (2) the fraction of inclusions is low and the interactions between the inclusions are neglected; (3) the boundary between inclusions and the host media is open such that LFF is allowed.

Denoting the spatial variables by x_i, $i = 1, 2, 3$, the displacement vector of the solid matrix by $\mathbf{u} = \left(u_1, u_2, u_3\right)^{\mathrm{T}}$, and the average fluid displacement vectors in the pores of the host media and inclusions by $\mathbf{U}^{(1)} = \left(U_1^{(1)}, U_2^{(1)}, U_3^{(1)}\right)^{\mathrm{T}}$ and $\mathbf{U}^{(2)} = \left(U_1^{(2)}, U_2^{(2)}, U_3^{(2)}\right)^{\mathrm{T}}$, respectively, the main governing equations are (Ba et al. 2011),

$$
\begin{aligned}
&N\nabla^2\mathbf{u} + (A + N)\nabla\varepsilon + Q_1\nabla\left(\zeta^{(1)} + \phi_2\varsigma\right) + Q_2\nabla\left(\zeta^{(2)} - \phi_1\varsigma\right) \\
&= \rho_{11}\ddot{\mathbf{u}} + \rho_{12}\ddot{\mathbf{U}}^{(1)} + \rho_{13}\ddot{\mathbf{U}}^{(2)} + b_1\left(\dot{\mathbf{u}} - \dot{\mathbf{U}}^{(1)}\right) + b_2\left(\dot{\mathbf{u}} - \dot{\mathbf{U}}^{(2)}\right),
\end{aligned} \tag{1a}
$$

$$
Q_1\nabla\varepsilon + R_1\nabla\left(\zeta^{(1)} + \phi_2\varsigma\right) = \rho_{12}\ddot{\mathbf{u}} + \rho_{22}\ddot{\mathbf{U}}^{(1)} - b_1\left(\dot{\mathbf{u}} - \dot{\mathbf{U}}^{(1)}\right), \tag{1b}
$$

$$
Q_2\nabla\varepsilon + R_2\nabla\left(\zeta^{(2)} - \phi_1\varsigma\right) = \rho_{13}\ddot{\mathbf{u}} + \rho_{33}\ddot{\mathbf{U}}^{(2)} - b_2\left(\dot{\mathbf{u}} - \dot{\mathbf{U}}^{(2)}\right), \tag{1c}
$$

$$
\begin{aligned}
&\phi_2\left(Q_1\varepsilon + R_1\left(\zeta^{(1)} + \phi_2\varsigma\right)\right) - \phi_1\left(Q_2\varepsilon + R_2\left(\zeta^{(2)} - \phi_1\varsigma\right)\right) \\
&= \frac{1}{3}\rho_f\ddot{\varsigma}R_0^2\frac{\phi_1^2\phi_2\phi_{20}}{\phi_{10}} + \frac{1}{3}\frac{\eta\phi_1^2\phi_2\phi_{20}}{\kappa_1}\dot{\varsigma}R_0^2,
\end{aligned} \tag{1d}
$$

where ε, $\zeta^{(1)}$, and $\zeta^{(2)}$ are the volume strains of the solid, fluid in the host medium, and fluid in the inclusions, respectively. They are the function of displacement vectors $\mathbf{u}$, $\mathbf{U}^{(1)}$, and $\mathbf{U}^{(2)}$ as follows,

$$
\varepsilon = \partial_i u_i, \zeta^{(1)} = \partial_i U_i^{(1)}, \zeta^{(2)} = \partial_i U_i^{(2)}, \tag{2}
$$

where ∂_i in Eq. (2) is the partial derivative with respect to the spatial variable x_i, and the Einstein convention over repeated indices is used. The dot above the variables in Eq. (1) represents the derivative with respect to the time variable. The equations involve six stiffness parameters (A, N, Q_1, Q_2, R_1, R_2), five density coefficients (ρ_{11}, ρ_{12}, ρ_{13}, ρ_{22}, ρ_{33}), three geometrical coefficients (ϕ_1, ϕ_2, R_0), the transport properties κ_1 and κ_2, and the fluid viscosity η. All these parameters can be estimated on the basis of measurable properties of the solid and fluid, and their detailed expressions are given in Appendix 1. Equation (1d) describes the LFF motion for the fluid strain's increment ς and is derived from a generalization of Rayleigh's theory of liquid collapse of a spherical cavity characterized by radius R_0 (Ba et al. 2011).

Equation (1) holds for uniform porosity, since the average displacements of the solid and fluid phases are used as Lagrangian coordinates and the respective stress components are used as generalized forces. Wang et al. (2019) further generalized these equations to the non-uniform porosity case. These variable-porosity equations are consistent with the boundary condition at interfaces separating media with different properties. In the non-uniform case, the constitutive relations for the total normal stress, shear stress and fluid pressures with respect to the solid and average fluid displacements $\mathbf{u}$, $\mathbf{U}^{(1)}$ and $\mathbf{U}^{(2)}$ are given by Wang et al. (2019).

$$\sigma_{ij} = \mu\left(\partial_i\partial u_j + \partial_j\partial u_i\right) + \delta_{ij}\left[\begin{array}{l}\left(\lambda_c - \alpha_1 M_1\phi_1 - \alpha_2 M_2\phi_2\right)\varepsilon + \alpha_1 M_1\phi_1\zeta^{(1)} \\ + \ \alpha_2 M_2\phi_2\zeta^{(2)} + \phi_1\phi_2\left(\alpha_1 M_1 - \alpha_2 M_2\right)\varsigma\end{array}\right], \tag{3}$$

$$P_{f1} = \left(-\alpha_1 M_1 + M_1\phi_1\right)\varepsilon - M_1\phi_1\zeta^{(1)} - M_1\phi_1\phi_2\varsigma, \tag{4}$$

$$P_{f2} = \left(-\alpha_2 M_2 + M_2\phi_2\right)\varepsilon - M_2\phi_2\zeta^{(2)} + M_2\phi_1\phi_2\varsigma, \tag{5}$$

where δ_{ij} is the Kronecker function. The related medium parameters for the variable-porosity equations are also given in Appendix 1. The Biot–Rayleigh equation for describing the LLF motion is then

$$\frac{\phi_{20}R_0^2}{3\phi_{10}}\left[\rho_f\phi_1\ddot{\varsigma} + b_1\dot{\varsigma}\right]$$
$$= \left[\left(\alpha_1 M_1 - \alpha_2 M_2 + M_2\phi_2 - M_1\phi_1\right)\varepsilon + M_1\phi_1\zeta^{(1)} - M_2\phi_2\zeta^{(2)} + \phi_1\phi_2\left(M_1 + M_2\right)\varsigma\right]. \tag{6}$$

3 Plane-Wave Solutions

For time harmonic oscillations (the Fourier convention is $e^{-i\omega t}$), the solution for Eq. (1d) is

$$\varsigma = \left[\left(\phi_1 Q_2 - \phi_2 Q_1\right)\varepsilon + R_2\phi_1\zeta^{(2)} - R_1\phi_2\zeta^{(1)}\right]/L, \tag{7}$$

where $L = R_1\phi_2^2 + R_2\phi_1^2 + \rho_f\omega^2 R_0^2\phi_1^2\phi_2\phi_{20}/\left(3\phi_{10}\right) + i\omega\eta\phi_1^2\phi_2\phi_{20}R_0^2/\left(3\kappa_1\right)$.

Substituting Eq. (7) into Eq. (1) and after a simplification, we obtain

$$\begin{pmatrix}\rho_{11} & \rho_{12} & \rho_{13} \\ \rho_{12} & \rho_{22} & 0 \\ \rho_{13} & 0 & \rho_{33}\end{pmatrix}\begin{pmatrix}\ddot{\mathbf{u}} \\ \ddot{\mathbf{U}}^{(1)} \\ \ddot{\mathbf{U}}^{(2)}\end{pmatrix} + \begin{pmatrix}b_1 + b_2 & -b_1 & -b_2 \\ -b_1 & b_1 & 0 \\ -b_2 & 0 & b_2\end{pmatrix}\begin{pmatrix}\dot{\mathbf{u}} \\ \dot{\mathbf{U}}^{(1)} \\ \dot{\mathbf{U}}^{(2)}\end{pmatrix}$$
$$= \begin{pmatrix}N\nabla^2 u + (A + N)\nabla\varepsilon + Q_1\nabla\zeta^{(1)} + Q_2\nabla\zeta^{(2)} + \left(Q_1\phi_2 - Q_2\phi_1\right)\nabla\varsigma \\ Q_1\nabla\varepsilon + R_1\nabla\zeta^{(1)} + R_1\phi_2\nabla\varsigma \\ Q_2\nabla\varepsilon + R_2\nabla\zeta^{(2)} - R_2\phi_1\nabla\varsigma\end{pmatrix}. \tag{8}$$

The three displacement vectors in Eq. (8) can be expressed in terms of potential functions with the aid of the Helmholtz decomposition,

$$\mathbf{u} = \nabla\varphi_s + \nabla \times \psi_s, \quad \mathbf{U}^{(1)} = \nabla\varphi_1 + \nabla \times \psi_1, \quad \mathbf{U}^{(2)} = \nabla\varphi_2 + \nabla \times \psi_2, \tag{9}$$

where φ_s and ψ_s are the potential functions of the solid-phase, φ_1 and ψ_1 are the potential functions of the fluid in the host matrix, while φ_2 and ψ_2 are the potential functions of the fluid in the inclusions.

After applying the Helmholtz decomposition, Eq. (8) becomes

$$
\begin{pmatrix} \rho_{11} & \rho_{12} & \rho_{13} \\ \rho_{12} & \rho_{22} & 0 \\ \rho_{13} & 0 & \rho_{33} \end{pmatrix} \begin{pmatrix} \ddot{\varphi}_s \\ \ddot{\varphi}_1 \\ \ddot{\varphi}_2 \end{pmatrix} + \begin{pmatrix} b_1 + b_2 & -b_1 & -b_2 \\ -b_1 & b_1 & 0 \\ -b_2 & 0 & b_2 \end{pmatrix} \begin{pmatrix} \dot{\varphi}_s \\ \dot{\varphi}_1 \\ \dot{\varphi}_2 \end{pmatrix}
$$
$$
= \begin{pmatrix} A + 2N - \frac{(Q_1\phi_2 - Q_2\phi_1)^2}{L} & Q_1 - \frac{R_1\phi_2(Q_1\phi_2 - Q_2\phi_1)}{L} & Q_2 + \frac{R_2\phi_1(Q_1\phi_2 - Q_2\phi_1)}{L} \\ Q_1 + R_1\phi_2(Q_2\phi_1 - Q_1\phi_2)/L & R_1 - (R_1\phi_2)^2/L & R_1\phi_2 R_2\phi_1/L \\ Q_2 - R_2\phi_1(Q_2\phi_1 - Q_1\phi_2)/L & R_1\phi_2 R_2\phi_1/L & R_2 - (R_2\phi_1)^2/L \end{pmatrix} \begin{pmatrix} \nabla^2\varphi_s \\ \nabla^2\varphi_1 \\ \nabla^2\varphi_2 \end{pmatrix}
$$

$$(10)$$

for the compressional waves, and

$$
\begin{pmatrix} \rho_{11} & \rho_{12} & \rho_{13} \\ \rho_{12} & \rho_{22} & 0 \\ \rho_{13} & 0 & \rho_{33} \end{pmatrix} \begin{pmatrix} \ddot{\psi}_s \\ \ddot{\psi}_1 \\ \ddot{\psi}_2 \end{pmatrix} + \begin{pmatrix} b_1 + b_2 & -b_1 & -b_2 \\ -b_1 & b_1 & 0 \\ -b_2 & 0 & b_2 \end{pmatrix} \begin{pmatrix} \dot{\psi}_s \\ \dot{\psi}_1 \\ \dot{\psi}_2 \end{pmatrix} = \nabla^2 \begin{pmatrix} N & 0 & 0 \\ 0 & 0 & 0 \\ 0 & 0 & 0 \end{pmatrix} \begin{pmatrix} \psi_s \\ \psi_1 \\ \psi_2 \end{pmatrix},
\qquad (11)
$$

for the shear wave.

The general plane-wave solutions for the potential functions in Eqs. (10) and (11) are

$$
\begin{pmatrix} \varphi_s \\ \varphi_1 \\ \varphi_2 \end{pmatrix} = \begin{pmatrix} A_s \exp\left(i\left(\mathbf{k_d} \cdot \mathbf{r} - \omega t\right)\right) \\ A_{f1} \exp\left(i\left(\mathbf{k_d} \cdot \mathbf{r} - \omega t\right)\right) \\ A_{f2} \exp\left(i\left(\mathbf{k_d} \cdot \mathbf{r} - \omega t\right)\right) \end{pmatrix},
\qquad (12a)
$$

$$
\begin{pmatrix} \psi_s \\ \psi_1 \\ \psi_2 \end{pmatrix} = \begin{pmatrix} B_s \exp\left(i\left(\mathbf{k_s} \cdot \mathbf{r} - \omega t\right)\right) \\ B_{f1} \exp\left(i\left(\mathbf{k_s} \cdot \mathbf{r} - \omega t\right)\right) \\ B_{f2} \exp\left(i\left(\mathbf{k_s} \cdot \mathbf{r} - \omega t\right)\right) \end{pmatrix},
\qquad (12b)
$$

where $\mathbf{k_d}$ and $\mathbf{k_s}$ are the complex wavenumber vectors for the compressional and shear waves, $\mathbf{r}$ is the location vector, and ω is the angular frequency. Because the fluid is viscous and the wave is inhomogeneous, the attenuation direction deviates from the propagation direction. Therefore, the wavenumber vectors $\mathbf{k_d}$ and $\mathbf{k_s}$ are the functions of the propagation direction, attenuation direction and the complex velocity for a given frequency.

Substituting Eq. (12a) into (10), and after a simplification, we obtain

$$
\begin{pmatrix} t_{11} & t_{12} & t_{13} \\ t_{21} & t_{22} & t_{23} \\ t_{31} & t_{32} & t_{33} \end{pmatrix} \begin{pmatrix} A_s \\ A_{f1} \\ A_{f2} \end{pmatrix} = \mathbf{T} \begin{pmatrix} A_s \\ A_{f1} \\ A_{f2} \end{pmatrix} = 0,
\qquad (13)
$$

where $\mathbf{T}$ is a symmetric 3×3 matrix with elements given by:

$$t_{11} = \rho_{11}\omega^2 + i\omega(b_1 + b_2) - \left(A + 2N - (Q_1\phi_2 - Q_2\phi_1)^2 \Big/ L\right)\mathbf{k_d^2},$$

$$t_{12} = t_{21} = \rho_{12}\omega^2 - i\omega b_1 - \left(Q_1 - R_1\phi_2(Q_1\phi_2 - Q_2\phi_1)/L\right)\mathbf{k_d^2},$$

$$t_{13} = t_{31} = \rho_{13}\omega^2 - i\omega b_2 - \left(Q_2 + R_2\phi_1(Q_1\phi_2 - Q_2\phi_1)/L\right)\mathbf{k_d^2},$$

$$t_{22} = \rho_{22}\omega^2 + i\omega b_1 - \left(R_1 - (R_1\phi_2)^2 \Big/ L\right)\mathbf{k_d^2},$$

$$t_{23} = t_{32} = - \left(R_1\phi_2 R_2\phi_1/L\right)\mathbf{k_d^2},$$

$$t_{33} = \rho_{33}\omega^2 + i\omega b_2 - \left(R_2 - (R_2\phi_1)^2 \Big/ L\right)\mathbf{k_d^2}.$$

In Eq. (13), the relation $\det(\mathbf{T}) = 0$ generates three complex wavenumbers (denoted as k_{p1}, k_{p2}, k_{p3}, respectively), corresponding to a fast P wave (P1) and two slow P waves (P2 and P3). By solving Eq. (13), the amplitude ratio between A_{f1} or A_{f2} and A_s can be determined as

$$\begin{pmatrix} A_{f1}/A_s \\ A_{f2}/A_s \end{pmatrix} = \begin{pmatrix} (t_{13}t_{21} - t_{11}t_{23})\big/(t_{12}t_{23} - t_{13}t_{22}) \\ (t_{11}t_{22} - t_{21}t_{12})\big/(t_{12}t_{23} - t_{13}t_{22}) \end{pmatrix}. \tag{14}$$

Similarly, substituting Eq. (12b) into (11) yields

$$\begin{pmatrix} q_{11} & q_{12} & q_{13} \\ q_{21} & q_{22} & q_{23} \\ q_{31} & q_{32} & q_{33} \end{pmatrix}\begin{pmatrix} B_s \\ B_{f1} \\ B_{f2} \end{pmatrix} = \mathbf{Q}\begin{pmatrix} B_s \\ B_{f1} \\ B_{f2} \end{pmatrix} = 0, \tag{15}$$

where $\mathbf{Q}$ is a symmetric 3×3 matrix with elements given by:

$$q_{11} = \rho_{11}\omega^2 + i\omega(b_1 + b_2) - N\mathbf{k_s^2},$$

$$q_{12} = q_{21} = \rho_{12}\omega^2 - i\omega b_1,$$

$$q_{13} = q_{31} = \rho_{13}\omega^2 - i\omega b_2,$$

$$q_{22} = \rho_{22}\omega^2 + i\omega b_1,$$

$$q_{23} = q_{32} = 0,$$

$$q_{33} = \rho_{33}\omega^2 + i\omega b_2.$$

In Eq. (15), the relation $\det(\mathbf{Q}) = 0$ gives only one physically meaningful complex wavenumber (denoted as k_s), corresponding to the shear wave (SV). By solving Eq. (15), the amplitude ratio between B_{f1} or B_{f2} and B_s can be determined as

$$\begin{pmatrix} B_{f1}/B_s \\ B_{f2}/B_s \end{pmatrix} = \begin{pmatrix} -q_{21}/q_{22} \\ (-q_{11}q_{22} + q_{21}q_{12})\big/(q_{13}q_{22}) \end{pmatrix}. \tag{16}$$

Once the complex wavenumbers are determined, the phase velocity and attenuation factor are (Carcione 2014)

Fig. 1 The reflection and transmission problem at a double-porosity interface. The solid and dashed arrows represent the propagation and attenuation directions, respectively. The inhomogeneity angle γ_0 is the angle between the attenuation and propagation directions
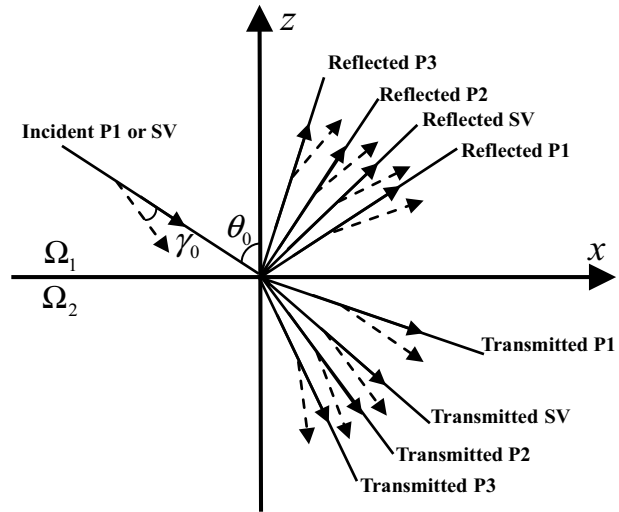
$$v_i = \left[\mathrm{Re}\{k_i/\omega\}\right]^{-1}, \tag{17}$$

$$Q_i^{-1} = 2\mathrm{Im}\{k_i\}/\mathrm{Re}\{k_i\}, \tag{18}$$

for $i = p1, p2, p3, s$. The symbols Re{} and Im{} indicate the real and imaginary parts of a complex variable, respectively.

4 Reflection and Transmission Coefficients

This study considers a 2D plane interface, defined by $z=0$, between two double-porosity media Ω_1 ($z>0$) and Ω_2 ($z<0$), and an inhomogeneous plane wave (P1 wave or SV wave, denoted with index 0) in Ω_1 incident at the interface with an oblique angle at a given angular frequency. The incident wave generates four reflected waves (P1, P2, P3, SV, denoted with the indexes 1, 2, 3, and 4, respectively) in Ω_1 and four transmitted waves (P1, P2, P3, SV, denoted with the indexes 5, 6, 7, and 8, respectively) in Ω_2. A scheme of the problem is illustrated in Fig. 1.

The double-porosity medium is saturated with viscous fluids and hence behaves anelastic, indicating that the waves in Fig. 1 are attenuated. Following Carcione (2014), the attenuated wave can be defined as inhomogeneous in general, in the sense that the propagation and attenuation directions are not the same. If these coincide, the wave is termed homogeneous. Given the propagation direction (θ_0), the inhomogeneity angle γ_0 (the angle between the attenuation and propagation directions) and the complex velocity, the incident inhomogeneous plane wave can be defined, and the corresponding potential functions for the solid-phase ϕ_s^0, the fluid-phase in the host matrix ϕ_{f1}^0, and the fluid-phase ϕ_{f2}^0 in the inclusions are

$$\begin{aligned}
\phi_s^i &= \phi_s^0 = A_s^0 \exp\left[i\omega\left(s_x^0 x + s_z^0 z\right) - i\omega t\right] \\
\phi_{f1}^i &= \phi_{f1}^0 = A_{f1}^0 \exp\left[i\omega\left(s_x^0 x + s_z^0 z\right) - i\omega t\right] \\
\phi_{f2}^i &= \phi_{f2}^0 = A_{f2}^0 \exp\left[i\omega\left(s_x^0 x + s_z^0 z\right) - i\omega t\right],
\end{aligned} \tag{19}$$

where s_x^0 and s_z^0 are the horizontal and vertical complex slowness. The horizontal slowness is given by Sharma (2013)

$$s_x^0 = \frac{|\mathbf{P}_0|}{\omega} \sin \theta_0 + i \frac{|\mathbf{A}_0|}{\omega} \sin (\theta_0 - \gamma_0). \tag{20}$$

The positive sign for $\mathrm{Re}\{s_x^0\}$ guarantees that the wave propagates along the positive x-direction. The magnitudes of the propagation vector $\mathbf{P}_0$ and attenuation vector $\mathbf{A}_0$ are

$$2|\mathbf{P}_0|^2 = \omega^2 \left[\mathrm{Re}\left(k_0^2/\omega^2\right) + \sqrt{\left(\mathrm{Re}\left(k_0^2/\omega^2\right)\right)^2 + \left(\mathrm{Im}\left(k_0^2/\omega^2\right)/\cos\gamma_0\right)^2} \right], \tag{21a}$$

$$2|\mathbf{A}_0|^2 = \omega^2 \left[-\mathrm{Re}\left(k_0^2/\omega^2\right) + \sqrt{\left(\mathrm{Re}\left(k_0^2/\omega^2\right)\right)^2 + \left(\mathrm{Im}\left(k_0^2/\omega^2\right)/\cos\gamma_0\right)^2} \right]. \tag{21b}$$

The vertical complex slowness s_z^0 is then determined as

$$s_z^0 = -d_R^0 - id_I^0, \quad d^0 = \pm p \cdot v \cdot \sqrt{\left(k_0^2/\omega^2\right) - \left(s_x^0\right)^2}, \tag{22}$$

where the symbol $p \cdot v\cdot$ represents the principal value of the complex quantity d^0. d_R^0 and d_I^0 represent the real and imaginary parts of d^0. The minus sign in $\mathrm{Re}\{s_z^0\}$ ensures that the incident wave propagates along the negative z-direction, while the minus sign in $\mathrm{Im}\{s_z^0\}$ ensures that the energy decays along the negative z-direction. The amplitude ratio between A_{f1}^0 or A_{f2}^0 and A_s^0 can be determined from Eq. (14) or (16) using the incident wavenumber k_0.

The potential functions of the reflected compressional waves in Ω_1 are

$$\phi_s^r = \sum_{l=1}^{3} \phi_s^l = \sum_{l=1}^{3} A_s^l \exp\left[i\omega\left(s_x^l x + s_z^l z\right) - i\omega t\right], \tag{23a}$$

$$\phi_{f1}^r = \sum_{l=1}^{3} \phi_{f1}^l = \sum_{l=1}^{3} A_{f1}^l \exp\left[i\omega\left(s_x^l x + s_z^l z\right) - i\omega t\right], \tag{23b}$$

$$\phi_{f2}^r = \sum_{l=1}^{3} \phi_{f2}^l = \sum_{l=1}^{3} A_{f2}^l \exp\left[i\omega\left(s_x^l x + s_z^l z\right) - i\omega t\right]. \tag{23c}$$

For the reflected shear wave in Ω_1, the expressions are

$$\begin{aligned} \psi_s^r &= \psi_s^4 = A_s^4 \exp\left[i\omega\left(s_x^4 x + s_z^4 z\right) - i\omega t\right] \\ \psi_{f1}^r &= \psi_{f1}^4 = A_{f1}^4 \exp\left[i\omega\left(s_x^4 x + s_z^4 z\right) - i\omega t\right] \\ \psi_{f2}^r &= \psi_{f2}^4 = A_{f2}^4 \exp\left[i\omega\left(s_x^4 x + s_z^4 z\right) - i\omega t\right]. \end{aligned} \tag{24}$$

The equations for the transmitted compressional waves in Ω_2 are

$$\phi_s^t = \sum_{l=5}^{7} \phi_s^l = \sum_{l=5}^{7} A_s^l \exp\left[i\omega\left(s_x^l x + s_z^l z\right) - i\omega t\right], \tag{25a}$$

$$\phi_{f1}^t = \sum_{l=5}^{7} \phi_{f1}^l = \sum_{l=5}^{7} A_{f1}^l \exp\left[i\omega\left(s_x^l x + s_z^l z\right) - i\omega t\right], \tag{25b}$$

$$\phi_{f2}^t = \sum_{l=5}^{7} \phi_{f2}^l = \sum_{l=5}^{7} A_{f2}^l \exp\left[i\omega\left(s_x^l x + s_z^l z\right) - i\omega t\right]. \tag{25c}$$

For the transmitted shear wave in Ω_2, we have

$$
\begin{aligned}
\psi_s^t &= \psi_s^8 = A_s^8 \exp\left[i\omega\left(s_x^8 x + s_z^8 z\right) - i\omega t\right] \\
\psi_{f1}^t &= \psi_{f1}^8 = A_{f1}^8 \exp\left[i\omega\left(s_x^8 x + s_z^8 z\right) - i\omega t\right] \\
\psi_{f2}^t &= \psi_{f2}^8 = A_{f2}^8 \exp\left[i\omega\left(s_x^8 x + s_z^8 z\right) - i\omega t\right].
\end{aligned}
\tag{26}
$$

According to the Snell's law, the horizontal slowness of all the reflected and transmitted waves is equal to that of the incident wave, which yields

$$s_x^0 = s_x^1 = s_x^2 = s_x^3 = s_x^4 = s_x^5 = s_x^6 = s_x^7 = s_x^8. \tag{27}$$

The vertical slowness of the reflected and transmitted compressional and shear waves is given by

$$s_z^l = d_R^l + id_I^l, \quad d^l = \pm p \cdot v \cdot \sqrt{\left(k_l^2/\omega^2\right) - \left(s_x^l\right)^2}, \quad l = 1, 2, 3, 4, \tag{28a}$$

$$s_z^l = -d_R^l - id_I^l, \quad d^l = \pm p \cdot v \cdot \sqrt{\left(k_l^2/\omega^2\right) - \left(s_x^l\right)^2}, \quad l = 5, 6, 7, 8. \tag{28b}$$

In medium Ω_1, the positive signs of $\mathrm{Re}\{s_z^l\}$ and $\mathrm{Im}\{s_z^l\}$ are chosen such that wave propagation is along the positive z-direction and the energy decays away from the interface. In medium Ω_2, the minus signs in $\mathrm{Re}\{s_z^l\}$ and $\mathrm{Im}\{s_z^l\}$ are chosen to ensure that the wave propagation is along the negative z-direction and the energy decays away from the interface.

The amplitude ratio between A_{f1}^l or A_{f2}^l and A_s^l in Eqs. (23)–(26) can be obtained by solving Eqs. (14) and (16) using the corresponding wavenumbers.

$$
\begin{pmatrix} A_{f1}^l / A_s^l \\ A_{f2}^l / A_s^l \end{pmatrix} = \left(\begin{array}{c} (t_{13}t_{21} - t_{11}t_{23})/(t_{12}t_{23} - t_{13}t_{22}) \\ (t_{11}t_{22} - t_{21}t_{12})/(t_{12}t_{23} - t_{13}t_{22}) \end{array} \right) = \begin{pmatrix} \delta_{f1s}^l \\ \delta_{f2s}^l \end{pmatrix} \text{ at } k = k_l, \quad \text{for } l = 1, 2, 3, 5, 6, 7.
\tag{29}
$$

$$
\begin{pmatrix} A_{f1}^l / A_s^l \\ A_{f2}^l / A_s^l \end{pmatrix} = \left(\begin{array}{c} -q_{21}/q_{22} \\ (-q_{11}q_{22} + q_{21}q_{12})/(q_{13}q_{22}) \end{array} \right) = \begin{pmatrix} \delta_{f1s}^l \\ \delta_{f2s}^l \end{pmatrix} \text{ at } k = k_l, \quad \text{for } l = 4, 8.
\tag{30}
$$

Using the above equations, the solid and average fluid displacements $\mathbf{u}$, $\mathbf{U}^{(1)}$ and $\mathbf{U}^{(2)}$ are expressed by

$$\mathbf{u}_I = \left(u_x^I, u_z^I\right) = \nabla\left(\sigma\phi_s^i + \phi_s^r\right) + \left(-\partial_z, \partial_x\right)\partial\left[(1 - \sigma)\phi_s^i + \psi_s^r\right], \tag{31a}$$

$$\mathbf{U}_I^{(1)} = \left(U_{1x}^I, U_{1z}^I\right) = \nabla\left(\sigma\phi_{f1}^i + \phi_{f1}^r\right) + \left(-\partial_z, \partial_x\right)\partial\left[(1-\sigma)\phi_{f1}^i + \psi_{f1}^r\right], \qquad (31b)$$

$$\mathbf{U}_I^{(2)} = \left(U_{2x}^I, U_{2z}^I\right) = \nabla\left(\sigma\phi_{f2}^i + \phi_{f2}^r\right) + \left(-\partial_z, \partial_x\right)\partial\left[(1-\sigma)\phi_{f2}^i + \psi_{f2}^r\right], \qquad (31c)$$

for medium Ω_1 and as

$$\mathbf{u}_{II} = \left(u_x^{II}, u_z^{II}\right) = \nabla\phi_s^t + \left(-\partial_z\partial\psi_s^t, \partial_x\partial\psi_s^t\right), \qquad (32a)$$

$$\mathbf{U}_{II}^{(1)} = \left(U_{1x}^{II}, U_{1z}^{II}\right) = \nabla\phi_{f1}^t + \left(-\partial_z\partial\psi_{f1}^t, \partial_x\partial\psi_{f1}^t\right), \qquad (32b)$$

$$\mathbf{U}_{II}^{(2)} = \left(U_{2x}^{II}, U_{2z}^{II}\right) = \nabla\phi_{f2}^t + \left(-\partial_z\partial\psi_{f2}^t, \partial_x\partial\psi_{f2}^t\right), \qquad (32c)$$

for medium Ω_2. The indexes I and II represent media Ω_1 and Ω_2, respectively. The parameter σ defines the incident P1 wave with $\sigma = 1$ and incident SV wave with $\sigma = 0$. The corresponding expressions for the solid stresses σ_{zz} and σ_{xz}, and fluid pressures P_{f1} and P_{f2} can then be derived from the non-uniform porosity Eqs. (3), (4), (5) and (7).

Many boundary conditions at the interface have been developed (Deresiewicz and Rice 1962, 1964; Dai et al. 2006a; Yeh et al. 2010; Sharma 2013; Kumar and Sharma 2013). Here we consider two boundary conditions (i.e., fully open and sealed) originally presented by Deresiewicz and Rice (1962, 1964). In case of a permeable boundary (i.e., the pores are fully open), the following continuity conditions should be satisfied at $z = 0$:

(1) Continuity of the z-component of solid displacement, $u_z^I = u_z^{II}$.

(2) Continuity of the x-component of solid displacement, $u_x^I = u_x^{II}$.

(3) Continuity of the total normal stress in the solid, $\sigma_{zz}^I = \sigma_{zz}^{II}$.

(4) Continuity of the total shear stress in the solid, $\sigma_{xz}^I = \sigma_{xz}^{II}$.

(5) Continuity of the rate of fluid flow in the host matrix, $\phi_1^I\left(U_{1z}^I - u_z^I\right) = \phi_1^{II}\left(U_{1z}^{II} - u_z^{II}\right)$.

(6) Continuity of the fluid pressure in the host matrix, $P_{f1}^I = P_{f1}^{II}$.

(7) Continuity of the rate of fluid flow in the inclusion, $\phi_2^I\left(U_{2z}^I - u_z^I\right) = \phi_2^{II}\left(U_{2z}^{II} - u_z^{II}\right)$.

(8) Continuity of the fluid pressure in the inclusion, $P_{f2}^I = P_{f2}^{II}$.

When the interface is assumed impermeable (i.e., the pores are sealed), there is no relative fluid flow across the boundary. The above boundary conditions (1)–(4) still hold, whereas the other four boundary conditions (5)–(8) become

(5) No fluid flow in the host matrix in medium Ω_1, $\phi_1^I\left(U_{1z}^I - u_z^I\right) = 0$.

(6) No fluid flow in the host matrix in medium Ω_2, $\phi_1^{II}\left(U_{1z}^{II} - u_z^{II}\right) = 0$.

(7) No fluid flow in the inclusion in medium Ω_1, $\phi_2^I\left(U_{2z}^I - u_z^I\right) = 0$.

(8) No fluid flow in the inclusion in medium Ω_2, $\phi_2^{II}\left(U_{2z}^{II} - u_z^{II}\right) = 0$.

Substituting the displacements and pressures into the boundary conditions and after a simplification using Snell's law, we obtain the following linear system of order eight,

$$[\mathbf{G}][\mathbf{x}] = \big[\mathbf{y}\big], \tag{33}$$

where $\mathbf{x}$ represents the ratio vector of the complex-value amplitudes to that of the incident wave defined by $\mathbf{x} = \big[x_l\big]_{l=1,\dots,8} = \big[A_s^l / A_s^0\big]_{l=1,\dots,8}$. The detailed expressions for the elements of $\mathbf{G}$ and $\mathbf{y}$ are given in Appendix 2.

The complex-value ratios in Eq. (33) can then be converted to the reflection and transmission coefficients as

$$R_l = \frac{A_s^l k_l}{A_s^0 k_0} = |R_l| e^{i\theta_l}, \ l = 1, 2, 3, 4, \tag{34a}$$

$$T_l = \frac{A_s^l k_l}{A_s^0 k_0} = |T_l| e^{i\theta_l}, \ l = 5, 6, 7, 8. \tag{34b}$$

The $|R_l|$ and $|T_l|$ are the absolute values of the complex quantities, R_l and T_l, and represent the reflection and transmission magnitudes, whereas the θ_l defines the respective phase angle (Dai et al. 2006a).

5 Energy partitions

The scalar product of the surface traction and the particle velocity represents the energy flux carried across the surface (Kumar and Saini 2012; Sharma 2013; Carcione 2014; Shekhar and Parvez 2016). For the double-porosity theory, the averaged energy intensity of a wave at the surface, with a normal along the z-direction, is given by

$$E = \frac{1}{2}\mathrm{Re}\big\{\sigma_{zz}\bar{\dot{u}}_z + \sigma_{xz}\bar{\dot{u}}_x - P_{f1}\bar{\dot{w}}_{1z} - P_{f2}\bar{\dot{w}}_{2z}\big\}, \tag{35}$$

where w_{1z} and w_{2z} are the displacements of the pore-fluid particles relative to the solid frame, defined by $w_{1z} = \phi_1\big(U_{1z} - u_z\big), w_{2z} = \phi_2\big(U_{2z} - u_z\big)$, and the bar denotes complex conjugate. In order to investigate the energy fluxes of the incident wave, reflected waves, and also their interactions in Ω_1, the following square matrix of order five is introduced,

$$\mathbf{E}_{\Omega_1} = \begin{bmatrix} E_{00} & E_{01} & E_{02} & E_{03} & E_{04} \\ E_{10} & E_{11} & E_{12} & E_{13} & E_{14} \\ E_{20} & E_{21} & E_{22} & E_{23} & E_{24} \\ E_{30} & E_{31} & E_{32} & E_{33} & E_{34} \\ E_{40} & E_{41} & E_{42} & E_{43} & E_{44} \end{bmatrix} = \frac{1}{2}\mathrm{Re}\big\{\mathbf{A}_{5x4}\bar{\mathbf{B}}_{4x5}\big\}, \tag{36}$$

where

$$\mathbf{A}_{5x4} = \begin{bmatrix} \sigma_{zz}^0 & \sigma_{xz}^0 & -P_{f1}^0 & -P_{f2}^0 \\ \sigma_{zz}^1 & \sigma_{xz}^1 & -P_{f1}^1 & -P_{f2}^1 \\ \sigma_{zz}^2 & \sigma_{xz}^2 & -P_{f1}^2 & -P_{f2}^2 \\ \sigma_{zz}^3 & \sigma_{xz}^3 & -P_{f1}^3 & -P_{f2}^3 \\ \sigma_{zz}^4 & \sigma_{xz}^4 & -P_{f1}^4 & -P_{f2}^4 \end{bmatrix}, \mathbf{B}_{4x5} = \begin{bmatrix} \dot{u}_z^0 & \dot{u}_z^1 & \dot{u}_z^2 & \dot{u}_z^3 & \dot{u}_z^4 \\ \dot{u}_x^0 & \dot{u}_x^1 & \dot{u}_x^2 & \dot{u}_x^3 & \dot{u}_x^4 \\ \dot{w}_{1z}^0 & \dot{w}_{1z}^1 & \dot{w}_{1z}^2 & \dot{w}_{1z}^3 & \dot{w}_{1z}^4 \\ \dot{w}_{2z}^0 & \dot{w}_{2z}^1 & \dot{w}_{2z}^2 & \dot{w}_{2z}^3 & \dot{w}_{2z}^4 \end{bmatrix}. \tag{37}$$

The diagonal entries E_{00}, E_{11}, E_{22}, E_{33} and E_{44} define the energy fluxes of the incident wave, and the reflected P1, P2, P3 and SV waves, respectively, while all the off-diagonal entries represent the interference energy fluxes among the incident wave, and reflected P1, P2, P3 and SV waves.

By applying Eqs. , (3)–(5), (31) and (32), the elements in matrix **A** and **B** can be further simplified as

$$\sigma_{zz}^l = A_s^l \omega^2 \left[\left(D_1^{\mathrm{I}} + D_2^{\mathrm{I}} \delta_{f1s}^l + D_3^{\mathrm{I}} \delta_{f2s}^l \right) \left(\left(s_x^l \right)^2 + \left(s_z^l \right)^2 \right) - 2\mu^{\mathrm{I}} \left(s_z^l \right)^2 \right], \tag{38a}$$

$$\sigma_{xz}^l = -A_s^l \omega^2 2\mu^{\mathrm{I}} s_x^l s_z^l, \tag{38b}$$

$$P_{f1}^l = A_s^l \omega^2 \left[\left(D_4^{\mathrm{I}} + D_5^{\mathrm{I}} \delta_{f1s}^l + D_6^{\mathrm{I}} \delta_{f2s}^l \right) \left(\left(s_x^l \right)^2 + \left(s_z^l \right)^2 \right) \right], \tag{38c}$$

$$P_{f2}^l = A_s^l \omega^2 \left[\left(D_7^{\mathrm{I}} + D_8^{\mathrm{I}} \delta_{f1s}^l + D_9^{\mathrm{I}} \delta_{f2s}^l \right) \left(\left(s_x^l \right)^2 + \left(s_z^l \right)^2 \right) \right], \tag{38d}$$

$$\dot{u}_x^l = A_s^l \omega^2 s_x^l, \tag{38e}$$

$$\dot{u}_z^l = A_s^l \omega^2 s_z^l, \tag{38f}$$

$$\dot{w}_{1z}^l = \phi_1^{\mathrm{I}} A_s^l \omega^2 \left(\delta_{f1s}^l - 1 \right) s_z^l, \tag{38g}$$

$$\dot{w}_{2z}^l = \phi_2^{\mathrm{I}} A_s^l \omega^2 \left(\delta_{f2s}^l - 1 \right) s_z^l, \tag{38h}$$

for $l = 1$, 2 and 3. The expressions for parameters $D_i^{\mathrm{I}} (i = 1, 2, \dots, 8, 9)$ are given in Appendix 3. The corresponding expressions for the shear wave are

$$\sigma_{zz}^l = -2A_s^l \omega^2 \mu^{\mathrm{I}} s_x^l s_z^l, \tag{39a}$$

$$\sigma_{xz}^l = -A_s^l \omega^2 \mu^{\mathrm{I}} \left[\left(s_x^l \right)^2 - \left(s_z^l \right)^2 \right], \tag{39b}$$

$$P_{f1}^l = 0, \tag{39c}$$

$$P_{f2}^l = 0, \tag{39d}$$

$$\dot{u}_x^l = -A_s^l \omega^2 s_z^l, \tag{39e}$$

$$\dot{u}_z^l = A_s^l \omega^2 s_x^l, \tag{39f}$$

$$\dot{w}_{1z}^l = \phi_1^{\mathrm{I}} A_s^l \omega^2 \left(\delta_{f1s}^l - 1 \right) s_x^l, \tag{39g}$$

$$\dot{w}_{2z}^l = \phi_2^{\mathrm{I}} A_s^l \omega^2 \left(\delta_{f2s}^l - 1 \right) s_x^l, \tag{39h}$$

with $l=4$. The corresponding expressions for the incident wave are dependent on the type of wave [i.e., Equation (38) with $l=0$ for the incident P1 wave, and Eq. (39) with $l=0$ for the incident SV wave].

Similarly, in Ω_2, the energy fluxes of the transmitted P1, P2, P3, and SV waves can be calculated as

$$\mathbf{E}_{\Omega_2} = \begin{bmatrix} E_{55} & E_{56} & E_{57} & E_{58} \\ E_{65} & E_{66} & E_{67} & E_{68} \\ E_{75} & E_{76} & E_{77} & E_{78} \\ E_{85} & E_{86} & E_{87} & E_{88} \end{bmatrix} = \frac{1}{2}\mathrm{Re}\{\mathbf{C}_{4x4}\bar{\mathbf{D}}_{4x4}\}, \tag{40}$$

where

$$\mathbf{C}_{4x4} = \begin{bmatrix} \sigma_{zz}^5 & \sigma_{xz}^5 & -P_{f1}^5 & -P_{f2}^5 \\ \sigma_{zz}^6 & \sigma_{xz}^6 & -P_{f1}^6 & -P_{f2}^6 \\ \sigma_{zz}^7 & \sigma_{xz}^7 & -P_{f1}^7 & -P_{f2}^7 \\ \sigma_{zz}^8 & \sigma_{xz}^8 & -P_{f1}^8 & -P_{f2}^8 \end{bmatrix}, \mathbf{D}_{4x4} = \begin{bmatrix} \dot{u}_z^5 & \dot{u}_z^6 & \dot{u}_z^7 & \dot{u}_z^8 \\ \dot{u}_x^5 & \dot{u}_x^6 & \dot{u}_x^7 & \dot{u}_x^8 \\ \dot{w}_{1z}^5 & \dot{w}_{1z}^6 & \dot{w}_{1z}^7 & \dot{w}_{1z}^8 \\ \dot{w}_{2z}^5 & \dot{w}_{2z}^6 & \dot{w}_{2z}^7 & \dot{w}_{2z}^8 \end{bmatrix}. \tag{41}$$

The corresponding expressions for $\sigma_{zz}^l, \sigma_{xz}^l, P_{f1}^l, P_{f2}^l, \dot{u}_x^l, \dot{u}_z^l, \dot{w}_{1z}^l, \dot{w}_{2z}^l$ with $l=5$, 6, and 7 are the same as Eq. (38) except using the parameters $D_i^{\mathrm{II}}, \mu^{\mathrm{II}}, \phi_1^{\mathrm{II}}$ and ϕ_2^{II}. In Eq. (39), instead of using parameters $\mu^{\mathrm{I}}, \phi_1^{\mathrm{I}}$ and ϕ_2^{I}, the expressions for the transmitted SV wave can be obtained by using $\mu^{\mathrm{II}}, \phi_1^{\mathrm{II}}$ and ϕ_2^{II}.

The reflected and transmitted energy fluxes E_{ii} are scaled to E_{00} to yield the reflected and transmitted energy ratios as follows,

$$\mathrm{RA}_{ii} = \frac{E_{ii}}{E_{00}}, \ (i=1,2,\dots,7,8). \tag{42}$$

The energy-ratio sum resulting from the interaction between the incident wave and the four reflected waves as well as interactions among the four reflected waves is given by
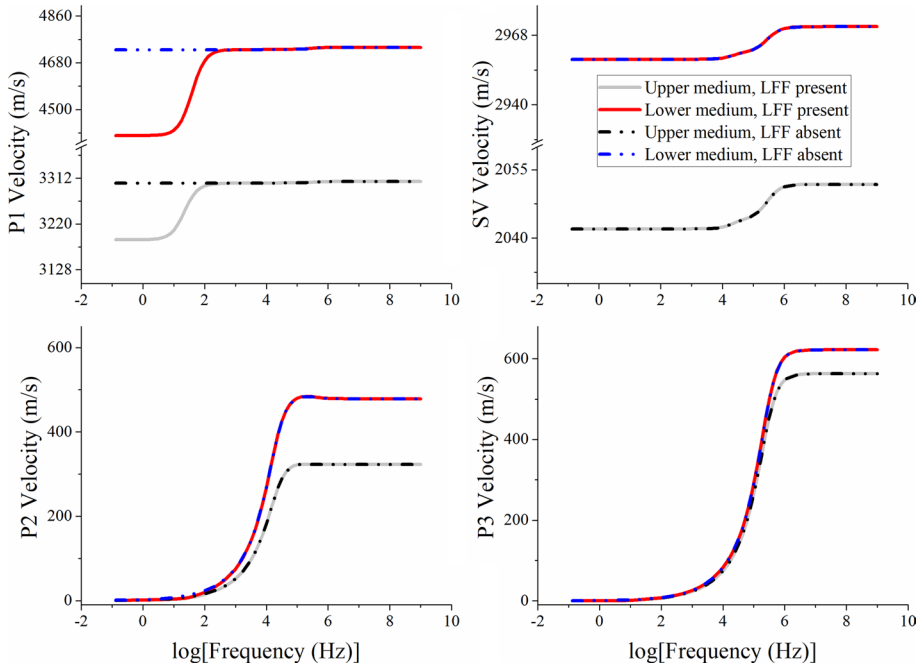
$$\mathrm{RA}_{ir} = \sum_{i=1}^4 \frac{E_{i0} + E_{0i}}{E_{00}} + \sum_{i=1}^4 \left(\sum_{j=1}^4 \frac{E_{ij}}{E_{00}} - \frac{E_{ii}}{E_{00}} \right). \tag{43}$$

Similarly, for the interactions among the four transmitted waves, the energy ratio sum is

$$\mathrm{RA}_{tt} = \sum_{i=5}^8 \left(\sum_{j=5}^8 \frac{E_{ij}}{E_{00}} - \frac{E_{ii}}{E_{00}} \right). \tag{44}$$

The conservation of the total energy at the stress-free surface can then be given by

$$\mathrm{RA}_{sum} = \sum_{i=1}^4 \mathrm{RA}_{ii} + \mathrm{RA}_{ir} - \sum_{i=5}^8 \mathrm{RA}_{ii} - \mathrm{RA}_{tt} = -1. \tag{45}$$
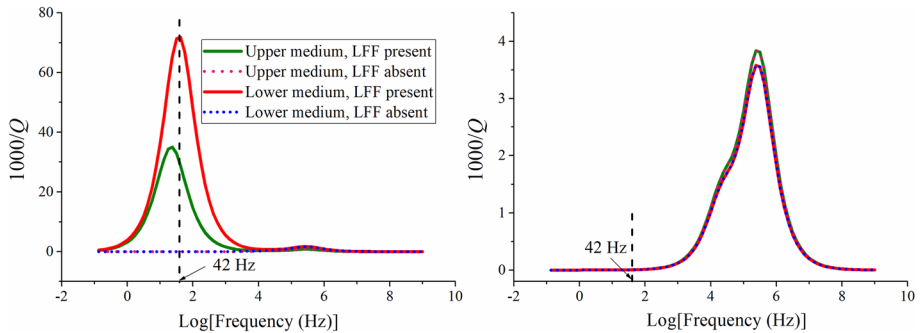
Fig. 2 Phase velocities of the P1, SV, slow P2, and slow P3 waves as a function of frequency. The red and gray solid lines correspond to the results of the lower and upper media with local fluid flow (LFF), whereas the blue and black dashed lines correspond to those of the lower and upper media without LFF

6 Examples

We consider the following medium properties of the upper and lower media:

Medium I: $\phi_{10}=0.1$, $\phi_{20}=0.3$, $v_1=0.963$, $\rho_s=2650$ kg/m^3, $\rho_f=1040$ kg/m^3, $K_s=18$ GPa, $K_f=2.5$ GPa, $\mu_s=24$ GPa, $c_1=10$, $c_2=200$, $c_s=10$, $R_0=0.02$ m, $\eta=0.001$ Pa s, $\kappa_1=0.01$ D, $\kappa_2=1$ D;

Fig. 3 Dissipation factors of the P1 wave (left) and SV wave (right) as a function of frequency. The red and olive solid lines correspond to the results of the lower and upper media with LFF, whereas the blue and red dashed lines correspond to those of the lower and upper media without LFF

Medium II: $\phi_{10}=0.1$, $\phi_{20}=0.3$, $v_1=0.963$, $\rho_s=2850$ kg/m³, $\rho_f=1040$ kg/m³, $K_s=48$ GPa, $K_f=2.5$ GPa, $\mu_s=54$ GPa, $c_1=10$, $c_2=200$, $c_s=10$, $R_0=0.02$ m, $\eta=0.001$ Pa s, $\kappa_1=0.01$ D, $\kappa_2=1$ D.

Most of the parameters given above are taken from Berryman and Wang (2000). The bulk and shear moduli are modified to introduce a stronger impedance contrast. In the following, the velocity dispersion and attenuation characteristics are firstly analyzed. Figure 2 shows the variations in phase velocities as a function of frequency. The dashed lines show the corresponding results when the LFF function is absent. The velocities are dependent on the frequency and are significantly affected by the LFF. In the presence
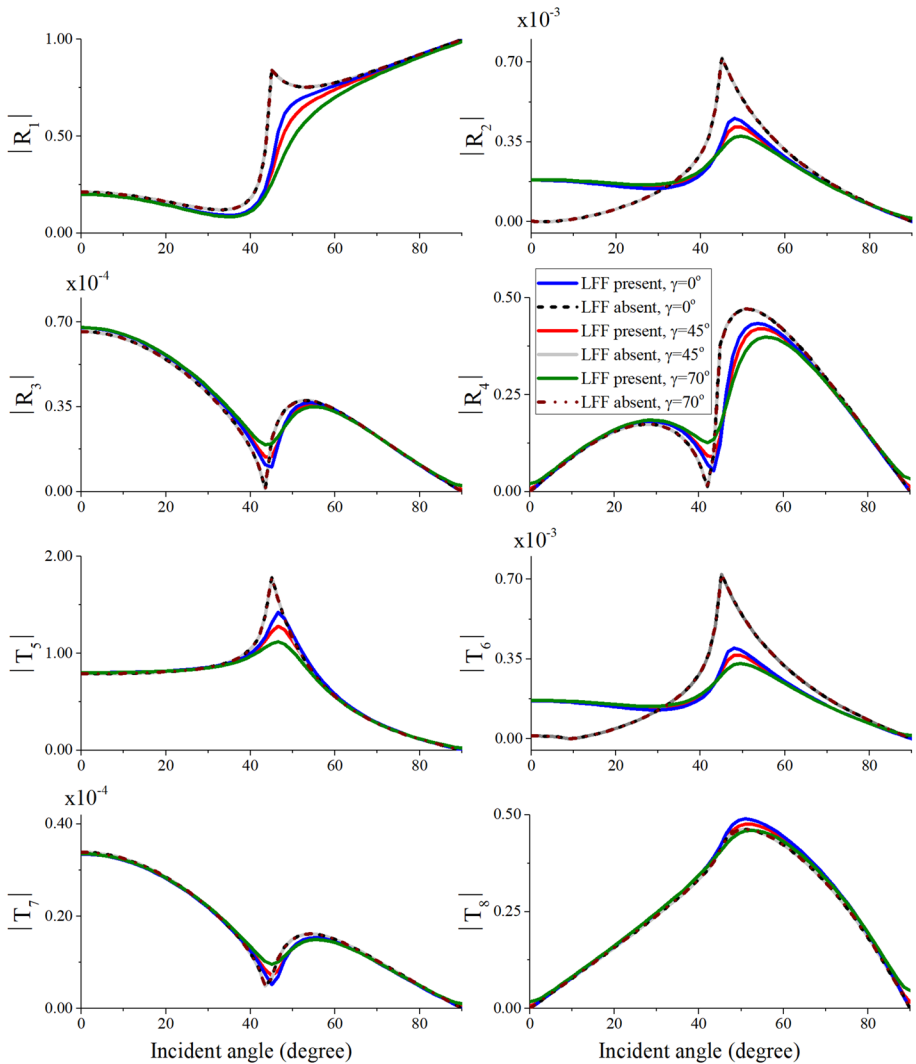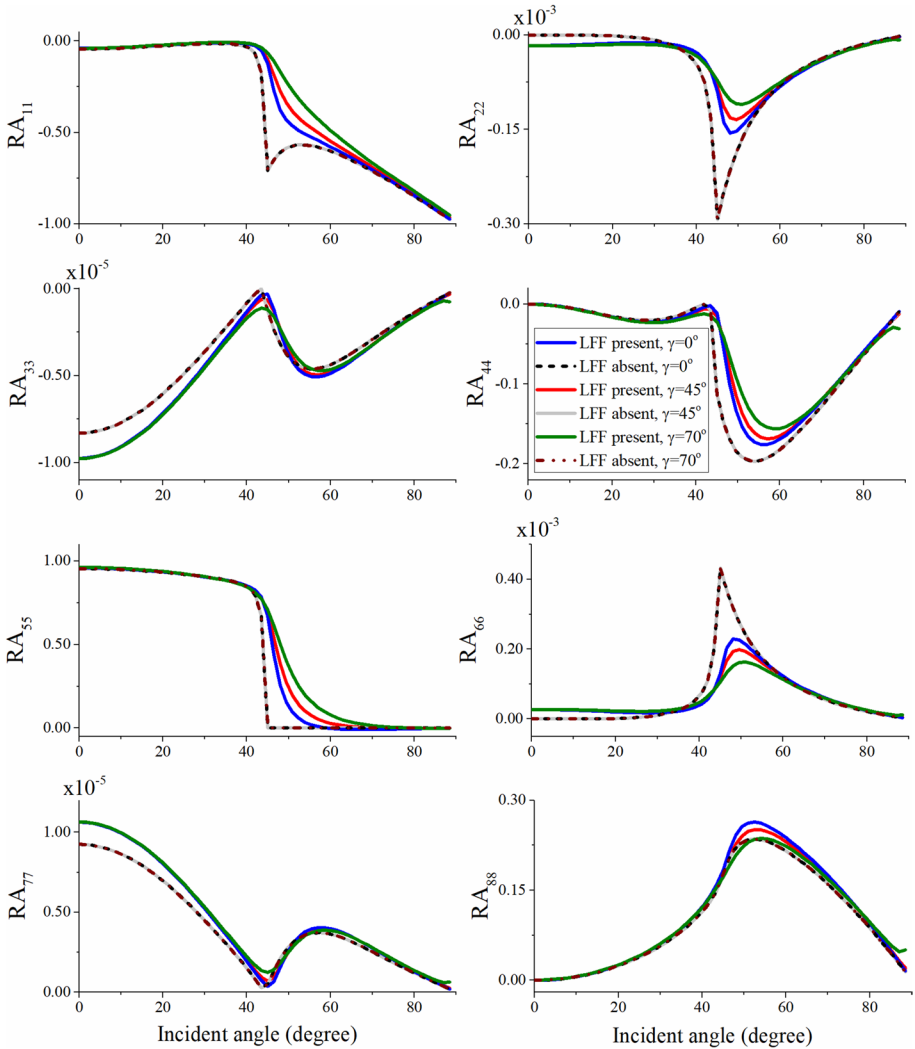

Fig. 4 Absolute value (magnitude) of the reflection and transmission coefficients as a function of the incidence angle at 42 Hz with different inhomogeneity angles, when the interface is open (incident P1 wave). Note that, when LFF is absent, the three curves are overlapped with each other
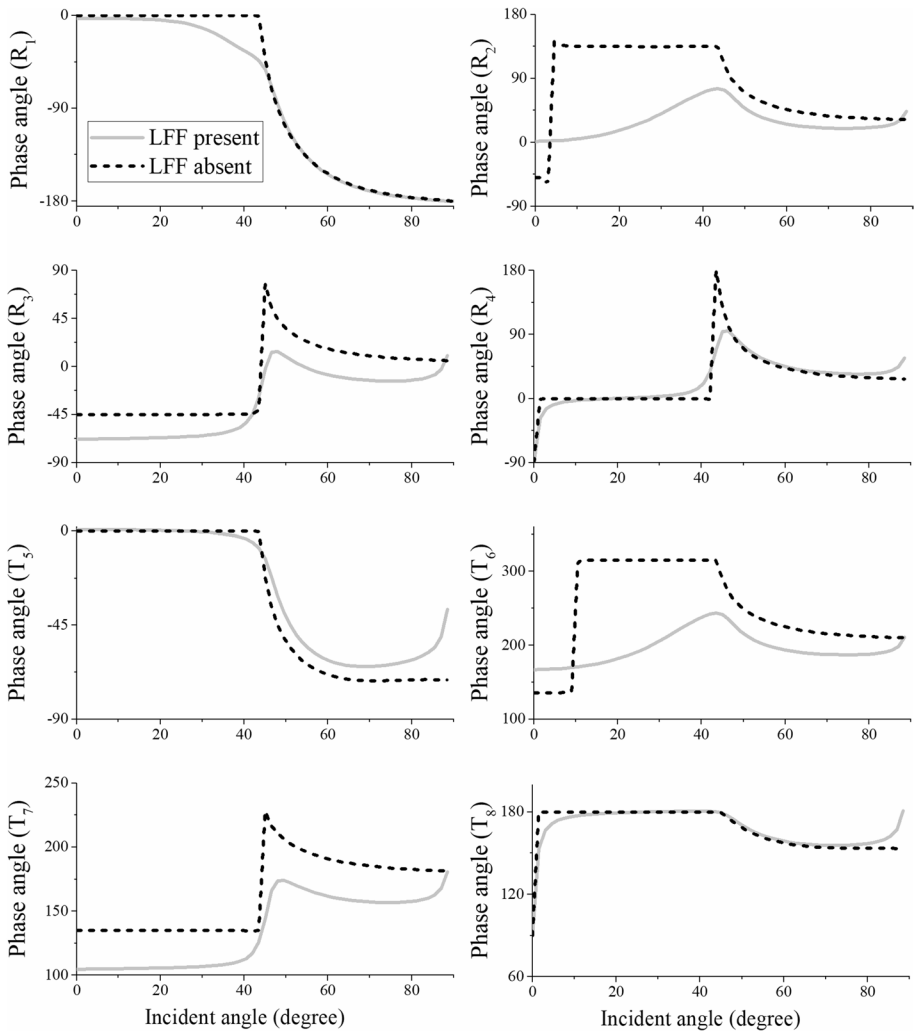
Fig. 5 Phases of the reflection and transmission coefficients as a function of the incidence angle at 42 Hz, when the interface is open (incident P1 wave). The inhomogeneity angle is at 45°

of it, the Biot–Rayleigh model predicts significant P1-wave velocity variations in the seismic frequency band from 10^{-1} to 10^3 Hz and can model velocity dispersion levels observed in rocks. By contrast, if the LFF effect is absent, the P1 phase velocity does not exhibit frequency dependence. The phase velocity of the SV wave is not affected by the LFF and exhibits an increase around a frequency of 100 kHz, resulting from the Biot loss mechanism. The phase velocities of the P2 and P3 waves are much smaller in comparison with those of the P1 and SV waves and are hardly affected by the LFF at all the frequencies. Figure 3 shows the dissipation factor as a function of frequency. Between 10^{-1} and 10^3 Hz, the presence of LFF induces significant attenuation of the P1 wave. The attenuation level is maximum at 42 Hz. In contrast, if the LFF is absent, no evident attenuation occurs. The dissipation factor of the SV wave is much smaller than that of

Fig. 6 Energy ratios as a function of the incidence angle at 42 Hz with different inhomogeneity angles, when the interface is open (incident P1 wave). Note that, when LFF is absent, the three curves are overlapped with each other

the P1 wave and exhibits a maximum around a frequency of 100 kHz, which is mainly induced by the Biot loss mechanism.
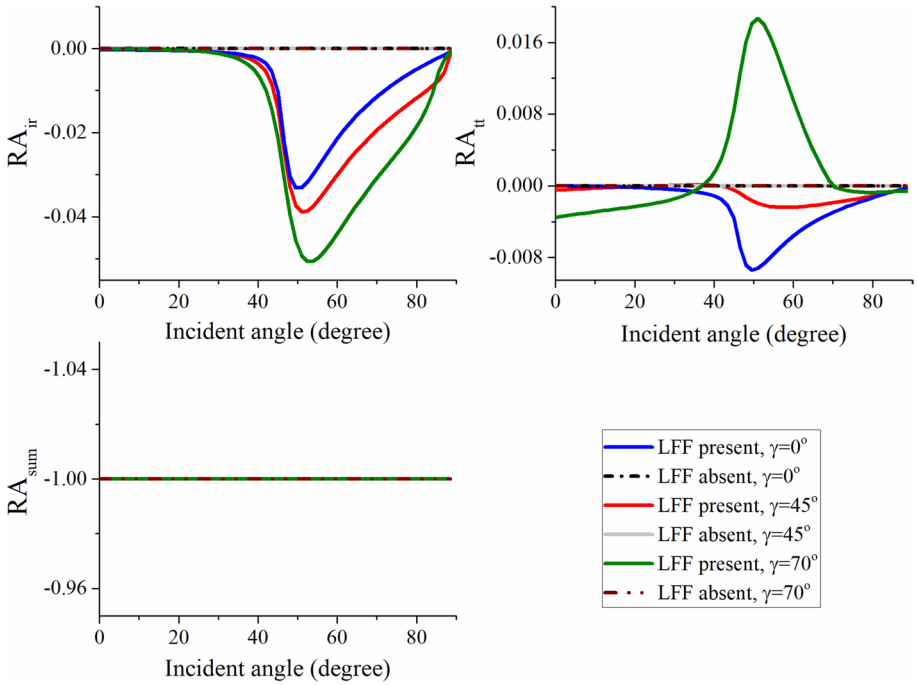
6.1 Incident P1 Wave

An incident P1 wave is first investigated. Three inhomogeneity angles at 0°, 45°, and 70° are considered. We use Eq. (33) to calculate the reflection and transmission coefficients and Eqs. (42), (43) and (44) to determine the corresponding energy ratios for both the open and sealed boundaries.

We first consider an open boundary. Figures 4 and 5 show the variations in the magnitude and phase of the reflection and transmission coefficients as a function of incidence angle. The corresponding energy-ratio variations are illustrated in Fig. 6. A frequency of 42 Hz is chosen such that the LFF effect is most evident. There exists a critical angle, but unlike in lossless media, all the velocities are complex and Snell's law may not yield a real critical angle. Actually, the critical angle in dissipative media is determined under the restrictions of the inhomogeneity angle and the quality factor (Borcherdt 1982). Rubino et al. (2006) alternatively defined a critical angle as the one beyond which the corresponding energy flux becomes zero. In this sense, with no LFF, the presence of a critical angle at 45° can be recognized from Fig. 6. This critical angle changes if LFF is present, because the P1-wave phase velocities in both layers are affected in this case.

The effect of LFF is visible, especially around the critical angle. This effect, regarding the magnitudes of the reflected and transmitted P1 waves, increases with oblique incidence and reaches a maximum at the critical angle. Beyond this angle, the effect decreases and disappears when approaching the grazing incidence. It causes a decrease in the magnitudes of both the reflected and transmitted P1 waves. The magnitude of the reflected SV wave is decreased in the presence of LFF for incidences beyond the critical. Whereas that of the transmitted SV wave is less affected and only exhibits a slight increase. In comparison with the P1 and SV waves, the magnitudes of P2 and P3 waves are smaller. The P2 waves have larger magnitudes than the P3 waves and are more evidently affected by the LFF. The presence of LFF enhances the magnitudes of reflected and transmitted P2 waves for small oblique incidences, but decreases these over large incidences, especially at the critical angle. As a contrast, the magnitudes of the reflected and transmitted P3 waves are only slightly affected by LFF for a small angle range around the critical. The LFF effect affects the phase angles as well, as shown in Fig. 5. For all incidence angles, the phases of all the waves vary continuously in the presence of LFF. If LFF is absent, they are constant for small incidence angles, specifically between 10° and the critical angle, and then exhibit a discontinuity at the critical angle.

The LFF induces energy attenuation of the P1 wave and consequently will affect the energy partitions, as illustrated by Fig. 6. The LFF effect on P1-wave energy is most evident at the critical angle and decreases toward the grazing incidence. When the LFF is absent, the medium behaves elastically at 42 Hz. In this case, beyond the critical, the transmitted P1 wave degenerates into a surface wave and travels along the interface, thus carrying no energy flux in the vertical direction. This explains the sudden disappearance of the energy of the transmitted P1 wave at the critical angle, as well as the sudden energy variation of the reflected P1 wave. However, if the LFF is present, the medium behaves anelastically, implying that the transmitted wave is not confined to the interface but propagates into the medium and hence it has vertical energy. This explains the continuous energy variation of the reflected and transmitted P1 waves in the presence of LFF. Meanwhile, beyond the critical angle, the LFF attenuates the energies of reflected P1 and SV waves, whereas it strengthens these of the transmitted P1 and SV waves. The reflected and transmitted P2 and P3 waves exhibit a much smaller energy. Before the critical angle, the LFF induces an energy increase, which becomes less significant toward the critical angle. This suggests that more energy transfer to the slow waves occurs when the LFF is present. Moreover, the LFF enhances the interference energy fluxes, as is shown in Fig. 7, whereas there is no interaction when without LFF. The same phenomenon has also been studied and illustrated in Sharma (2013). The sum of all the energy ratios at the interface is -1.0 for all incidence angles, indicating that the conservation of energy is satisfied.

Fig. 7 Interference fluxes and sum of the energy ratio at 42 Hz with different inhomogeneity angles, when the interface is open (incident P1 wave). Note that, when LFF is absent, the three curves are overlapped with each other
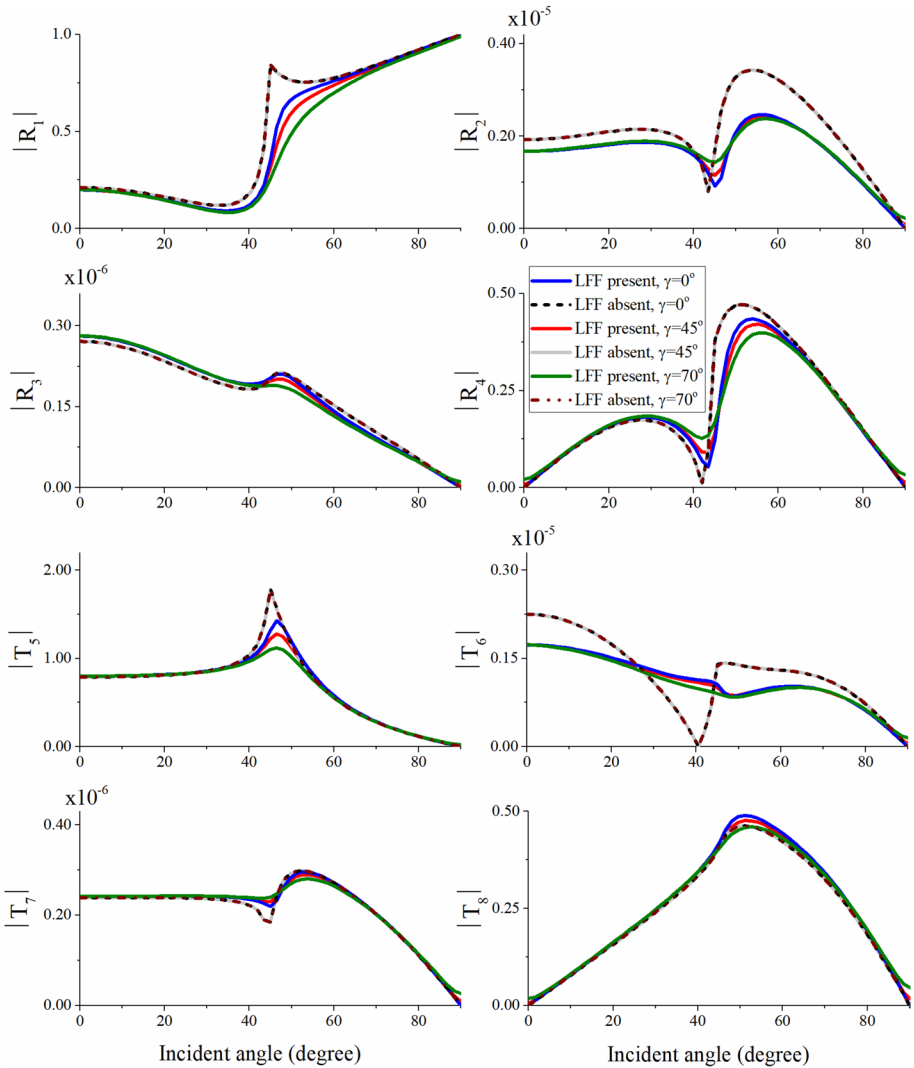
If the LFF is absent, reflection and transmission are not affected by γ_0. As shown in Fig. 3, the dissipation factor, defined by Eq. (18), is zero at 42 Hz. In this case, we have,

$$\frac{\text{Im}\left\{(k_i)^2\right\}}{\text{Re}\left\{(k_i)^2\right\}} = \frac{2\text{Im}\{k_i\}/\text{Re}\{k_i\}}{1 - [\text{Im}\{k_i\}/\text{Re}\{k_i\}]^2} = \frac{Q_i^{-1}}{1 - Q_i^{-2}/4} \approx 0. \quad (46)$$

With Eq. (46), the magnitudes of the propagation and attenuation vectors are

$$2|\mathbf{P}_0|^2 = \omega^2 \text{Re}\left(k_0^2/\omega^2\right)\left[1 + \sqrt{1 + \left(\frac{\text{Im}\left(k_0^2/\omega^2\right)}{\text{Re}\left(k_0^2/\omega^2\right)}\right)^2 \frac{1}{(\cos\gamma_0)^2}}\right] \approx 2\omega^2 \text{Re}\left(k_0^2/\omega^2\right),$$

$$(47a)$$

$$2|\mathbf{A}_0|^2 = \omega^2 \text{Re}\left(k_0^2/\omega^2\right)\left[-1 + \sqrt{1 + \left(\frac{\text{Im}\left(k_0^2/\omega^2\right)}{\text{Re}\left(k_0^2/\omega^2\right)}\right)^2 \frac{1}{(\cos\gamma_0)^2}}\right] \approx 0. \quad (47b)$$

Fig. 8 Absolute value (magnitude) of the reflection and transmission coefficients as a function of the incidence angle at 42 Hz with different inhomogeneity angles, when the interface is sealed (incident P1 wave). The three curves are overlapped with each other when LFF is absent

Using Eq. (47), the wavenumber of the incident wave defined in Eq. (20) as a function of $|\mathbf{P}_0|$ and $|\mathbf{A}_0|$ is independent of γ_0, if the LFF is absent. Since the incident wave is not affected by γ_0, reflection and transmission behaviors are not affected. If the LFF effect is present, Q_i^{-1} is not zero, a consequence of non-zero $\mathrm{Im}\left\{(k_i)^2\right\} \big/ \mathrm{Re}\left\{(k_i)^2\right\}$ in Eq. (46). This leads to the dependence of both $|\mathbf{P}_0|$ and $|\mathbf{A}_0|$ on γ_0. In this case, the inhomogeneity angle γ_0 affects the incident wave, and also the reflected and transmitted fields. The effect is mainly observed at post-critical incidences. The increase of γ_0 leads to an increasing $|\mathbf{A}_0|$ and consequently yields a decrease in the magnitudes of the reflected and transmitted P1
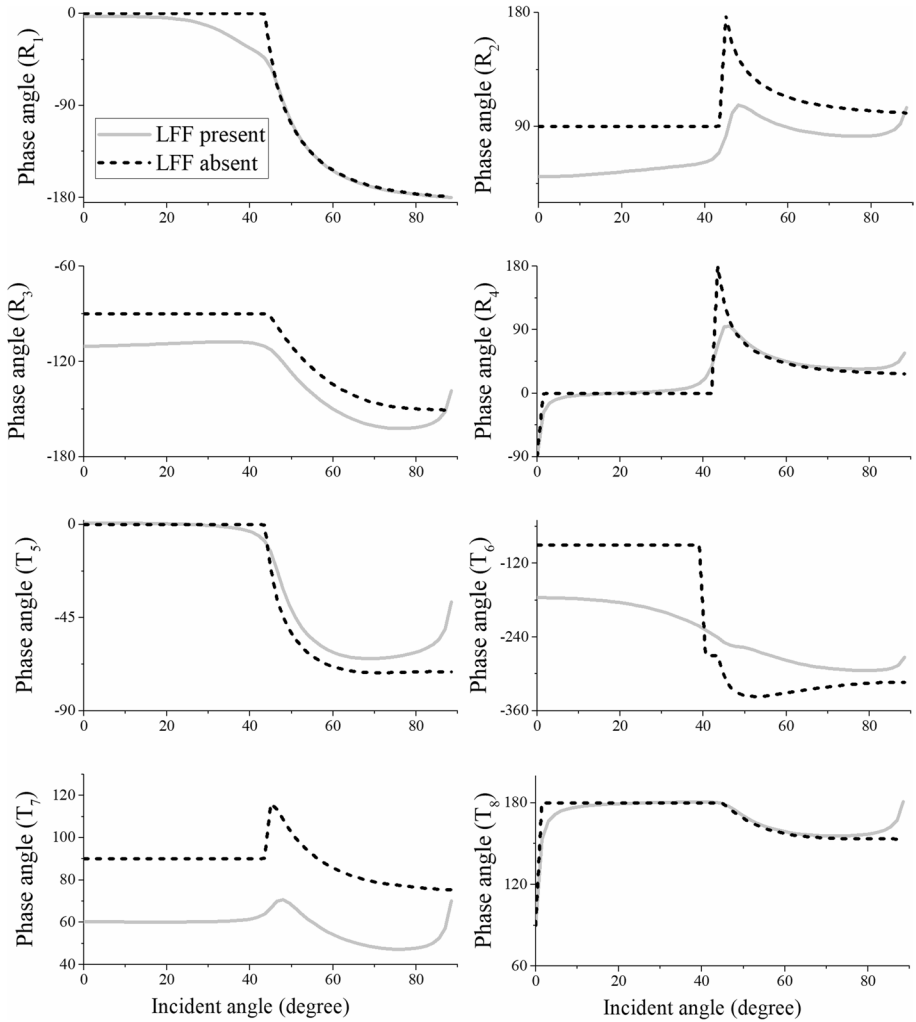
Fig. 9 Phases of the reflection and transmission coefficients as a function of the incidence angle at 42 Hz, when the interface is sealed (incident P1 wave). The inhomogeneity angle is at 45°

and SV waves. It also induces increased interference energy fluxes between the incident and reflected waves at post-critical incidences.

Next, the sealed boundary is considered. The variations in magnitudes, phases and energy ratios are given in Figs. 8, 9 and 10. The same critical angle as aforementioned occurs. Compared to Figs. 4 and 5, the magnitudes and phases of P1 and SV coefficients are kept the same, whereas those of the P2 and P3 coefficients change. The magnitudes are reduced and the variation trends change. In comparison with P3 waves, the reflected and transmitted P2 waves are more affected by the LFF. Its presence causes a visible decrease in the P2-wave magnitudes for most of the incidence angles. Furthermore, their phases are significantly affected. The inhomogeneity angle γ_0 affects the behavior of the reflected and transmitted P1 and SV waves in the same manner as in the case of open boundary.
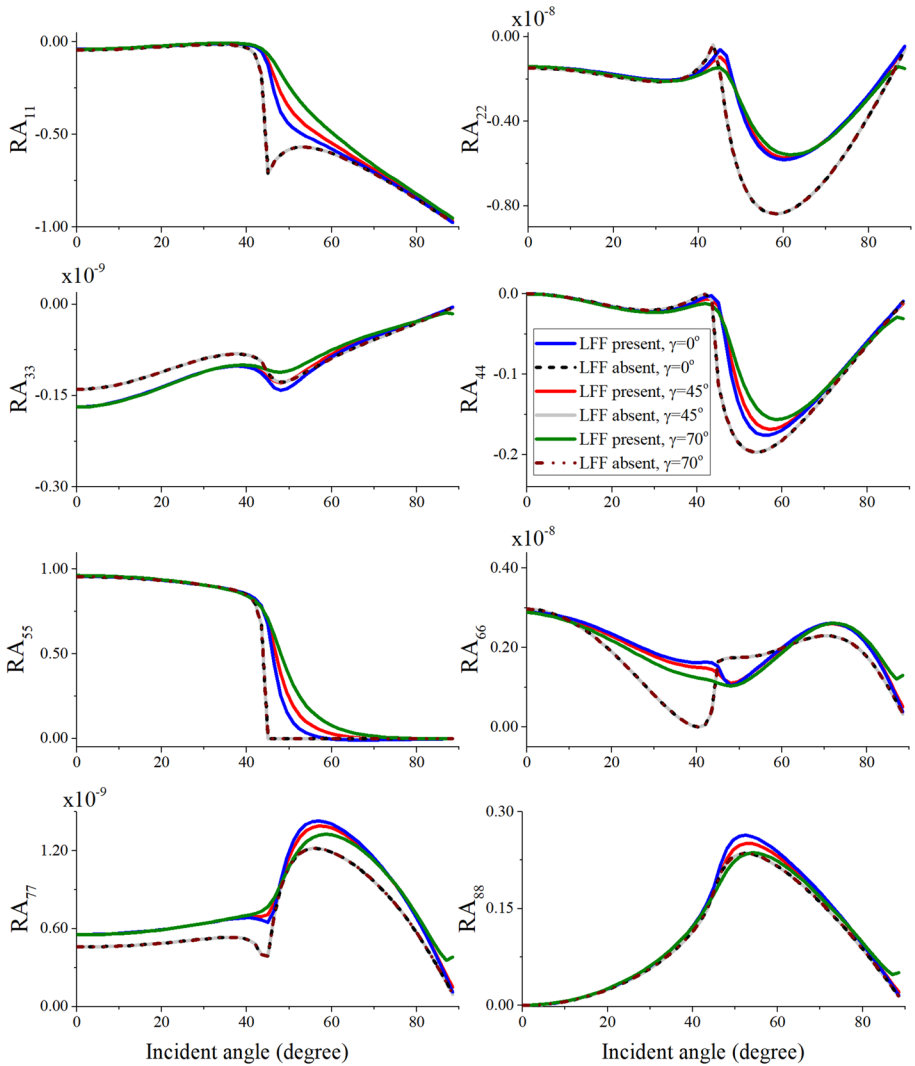
Fig. 10 Energy ratios as a function of the incidence angle at 42 Hz with different inhomogeneity angles, when the interface is sealed (incident P1 wave). When LFF is absent, the three curves are overlapped with each other

The sealing boundary does not affect the energy ratios of the P1 and SV waves for the given inhomogeneity angle γ_0, as is illustrated in Fig. 10, but significantly influences those of the P2 and P3 waves. In comparison with Fig. 6, the sealing boundary reduces the energies of the P2 and P3 waves. Below the critical angle, the presence of LFF strengthens the energies of the reflected P3, transmitted P2, and transmitted P3 waves, implying that more energy conversion to slow wave modes occurs. For post-critical incidences, the LFF evidently enhances the transmitted P3 wave but weakens the reflected P2 wave. The interference energy fluxes and sum in this case are similar as those given in Fig. 7.
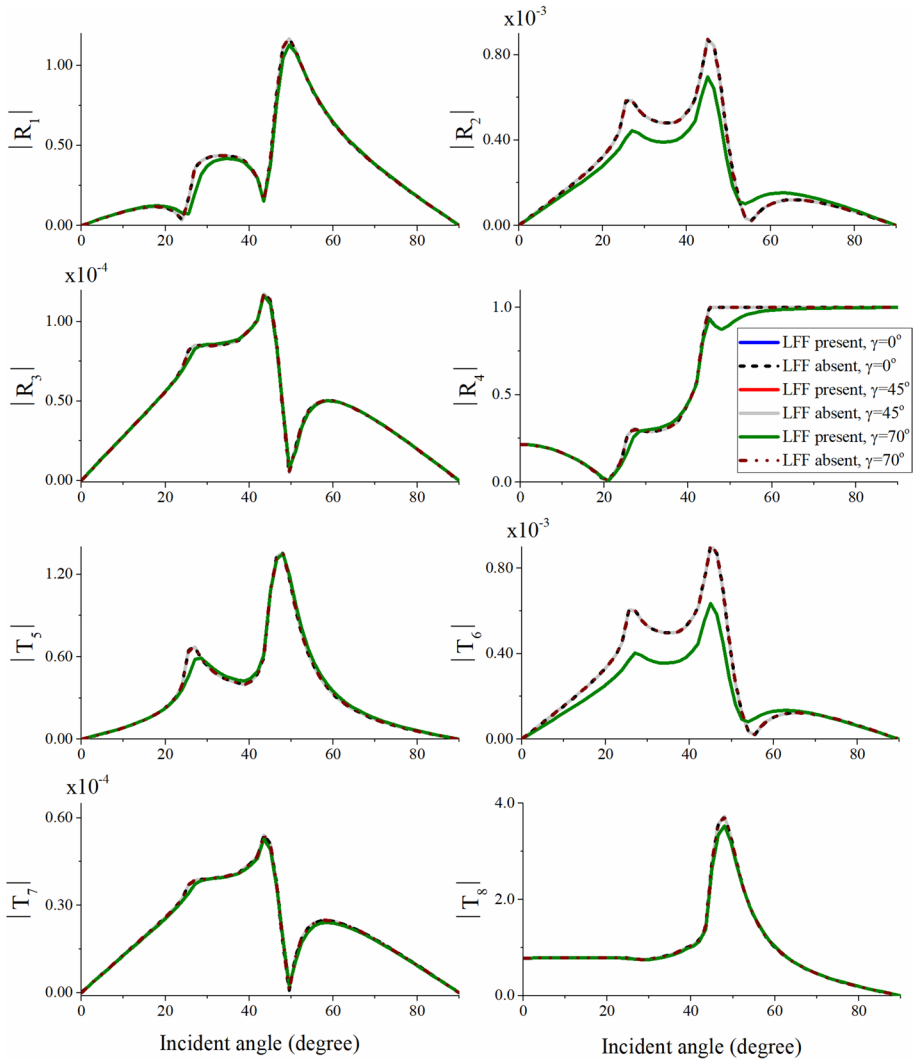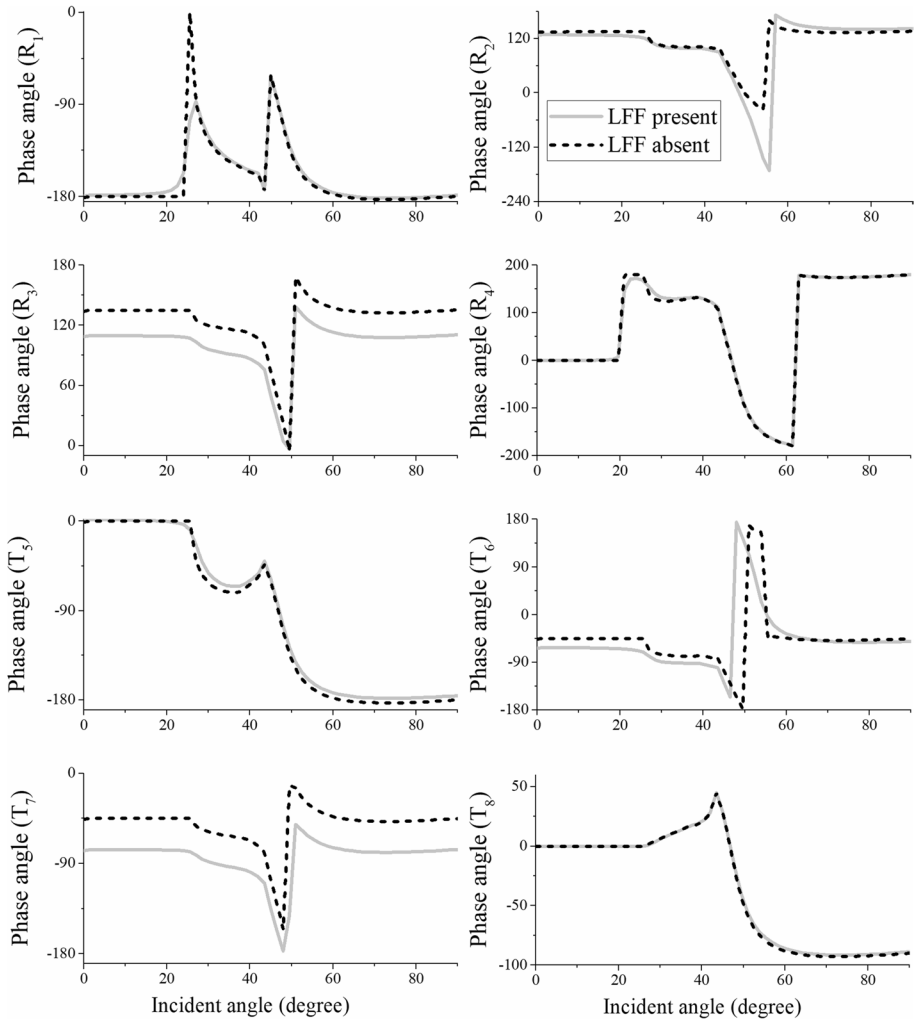
Fig. 11 Absolute value (magnitude) of the reflection and transmission coefficients as a function of the incidence angle at 42 Hz with different inhomogeneity angles, when the interface is open (incident SV wave). Note that, irrespective of the LFF being absent or present, the corresponding three curves with different inhomogeneity angles overlap

6.2 Incident SV Wave

The SV-wave incidence with three different inhomogeneity angles at 0°, 45°, and 70° is considered, with both open and sealed boundaries.

The open boundary is first studied. Figures 11, 12, and 13 show the variations in magnitudes, phases, and energy ratios of the reflection and transmission coefficients at 42 Hz. It can be observed that the inhomogeneity angle γ_0 does not affect the reflected and transmitted fields, irrespective if the LFF is present or absent. The explanations are similar to

Fig. 12 Phases of the reflection and transmission coefficients as a function of the incidence angle at 42 Hz, when the interface is open (incident SV wave). The inhomogeneity angle is at 45°

those of the examples related to the P1-wave incidence without LFF. The dissipation factor Q^{-1} of the SV wave at 42 Hz is zero. Therefore, the incident SV wave with the wavenumber defined in Eq. (20) as a function of $|\mathbf{P}_0|$ and $|\mathbf{A}_0|$ is not affected by γ_0. The effect of LFF on the reflection and transmission behaviors is not as significant as those yielded from P1-wave incidence. Two critical angles associated to the P1 and SV waves at about 25° (the first) and 45° (the second) can be recognized, where the magnitudes, phases, and energies exhibit most evident change. At the two critical angles, the magnitude of the reflected P1 wave exhibits two minima, whereas that of the transmitted P1 wave has peaks. The LFF effect noticeably induces a decrease in magnitude of the P1 wave only between the two critical angles. The magnitudes of the two slow waves are not so significant. The LFF decreases the magnitudes of the reflected and transmitted P2 waves, whereas it hardly affects those of the P3 waves. This effect is most evident at the two critical angles. The LFF
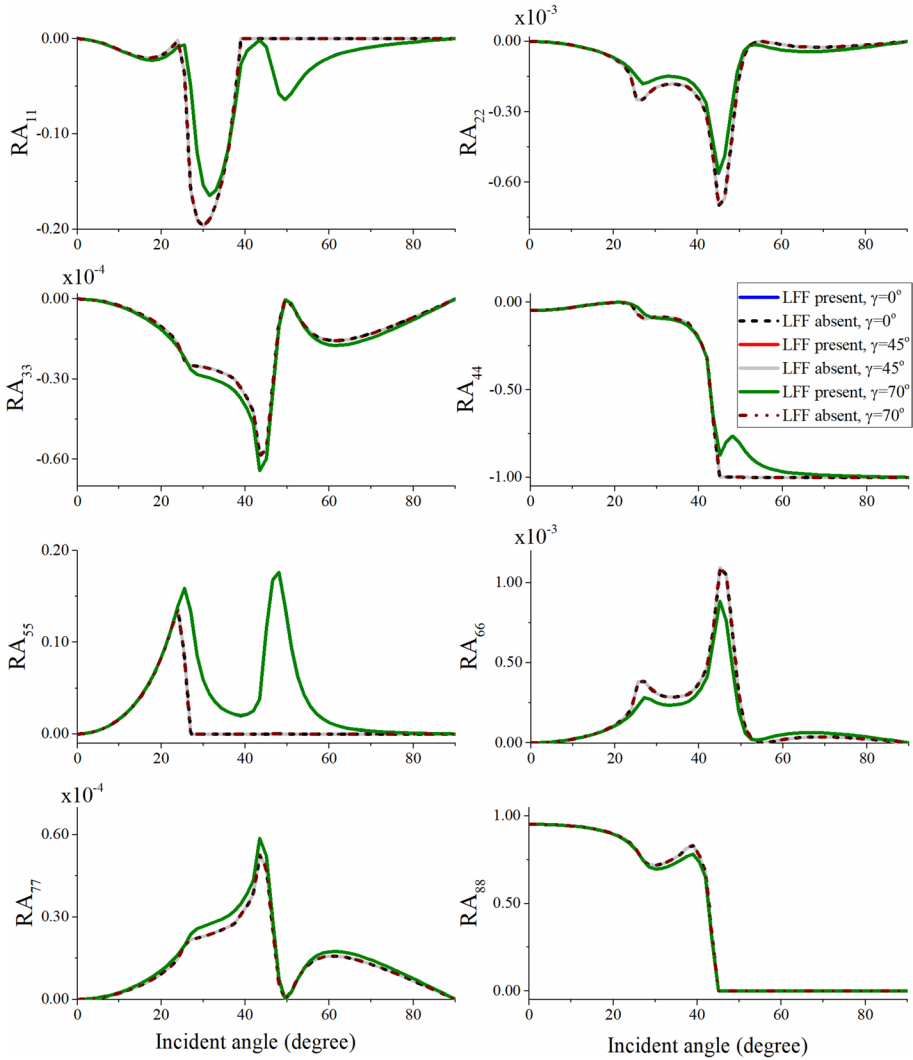
Fig. 13 Energy ratios as a function of the incidence angle at 42 Hz with different inhomogeneity angles, when the interface is open (incident SV wave). Irrespective of the LFF being absent or present, the corresponding three curves with different inhomogeneity angles overlap

effect affects the phases as well, especially these of the P2 and P3 waves. At the two critical angles, the phase varies most evidently.

The LFF affects the reflected and transmitted P1 waves, thus affects the energy partitions, as is given in Fig. 13. The main energy goes to the transmitted SV wave below the second critical angle, and to the reflected SV wave beyond that angle. When the LFF effect is absent, the P1 wave is not attenuated. In this case, the transmitted P1 wave degenerates into a surface wave and travels along the interface for post-critical incidence angles. Thus, its energy decreases to zero rapidly. If the LFF effect is present, the transmitted wave is attenuated and propagates into the medium. Therefore, it carries energy, as predicted by the energy ratio RA_{55} displayed
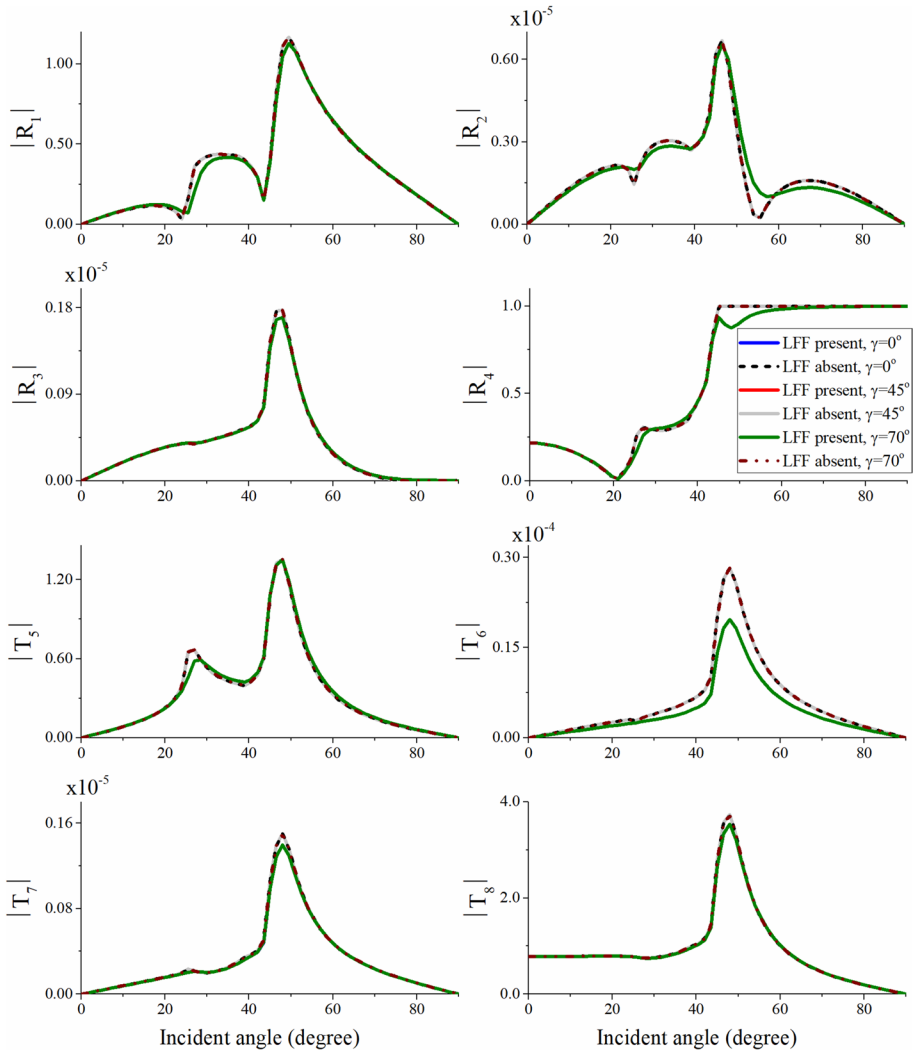
Fig. 14 Absolute value (magnitude) of the reflection and transmission coefficients as a function of the incidence angle at 42 Hz with different inhomogeneity angles, when the interface is sealed (incident SV wave). Irrespective of the LFF being absent or present, the corresponding three curves with different inhomogeneity angles are overlapped with each other

in Fig. 13. As a consequence, the energy of reflected P1 wave is influenced, which exhibits an increase beyond the second critical angle. The enhanced energy shared by the reflected and transmitted P1 waves beyond the second critical angle explains the reason of energy decrease in the reflected SV wave in the presence of LFF. Similar to the magnitudes, the energy ratios of P2 and P3 waves are not so much significant. Peaks at the two critical angles can be observed, affected by the LFF. The LFF implies an energy decrease in the reflected and transmitted P2 waves, whereas it increases the energy of the reflected and transmitted P3 waves. A possible explanation is that part of the P2-wave energy is converted to the P3 wave. The sum of all the energy ratios is -1.0 for all angles, which verifies the energy conservation at the interface.
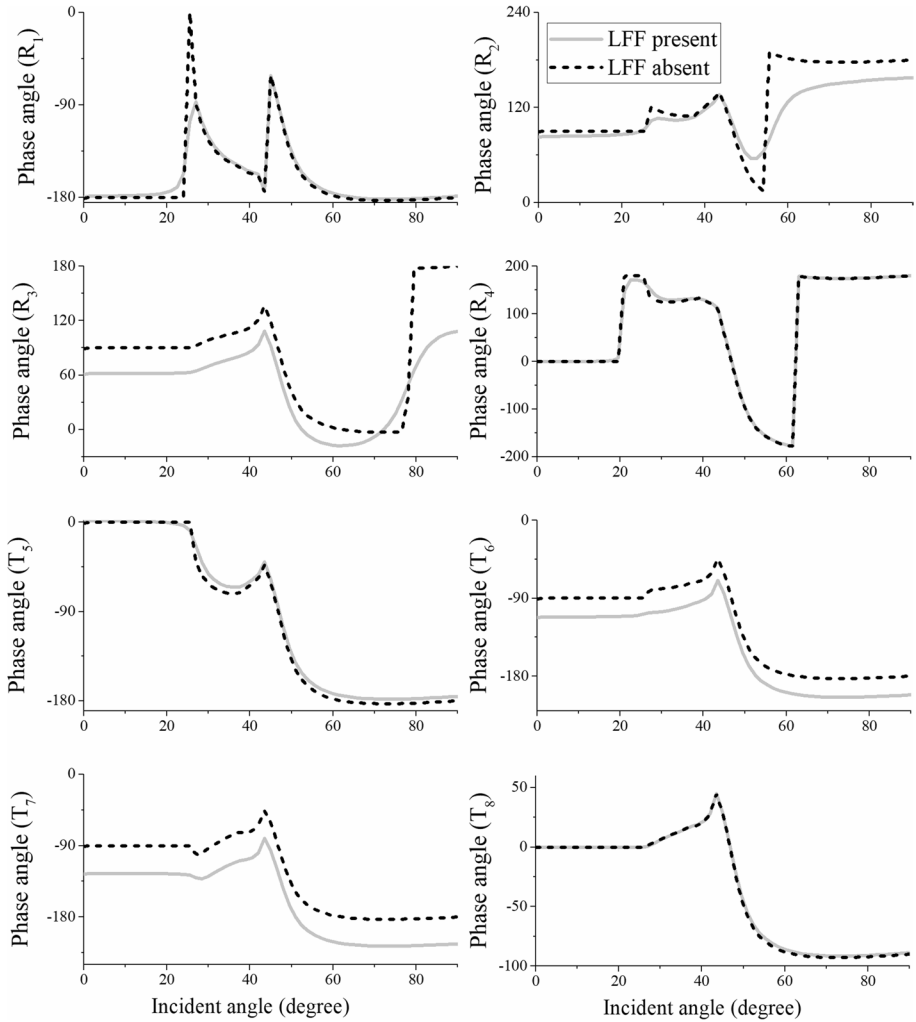
Fig. 15 Phases of the reflection and transmission coefficients as a function of the incidence angle at 42 Hz, when the interface is sealed (incident SV wave). The inhomogeneity angle is at 45°

Next, the sealed boundary is considered. Figures 14, 15, and 16 show the variations in the magnitudes, phases, and energies. Similar to the P1 incidence, the change of sealing boundary does not influence the behaviors of reflected and transmitted P1 and SV waves, but affects these of P2 and P3 waves significantly, including the magnitudes, phases, and the energies. The presence of LFF decreases the magnitude of transmitted P2 wave for nearly all incidences. However, it hardly affects these of the reflected and transmitted P3 wave. The energy shares of the reflected and transmitted P2 and P3 waves become more insignificant due to the sealing boundary. The LFF effect enhances the reflected P2 wave, but weakens the transmitted P2 wave. On the contrary, the P3 wave is not visibly affected. The sum of the energy ratios including the interference is −1.0 for all incidences, which confirms the conservation at the surface.
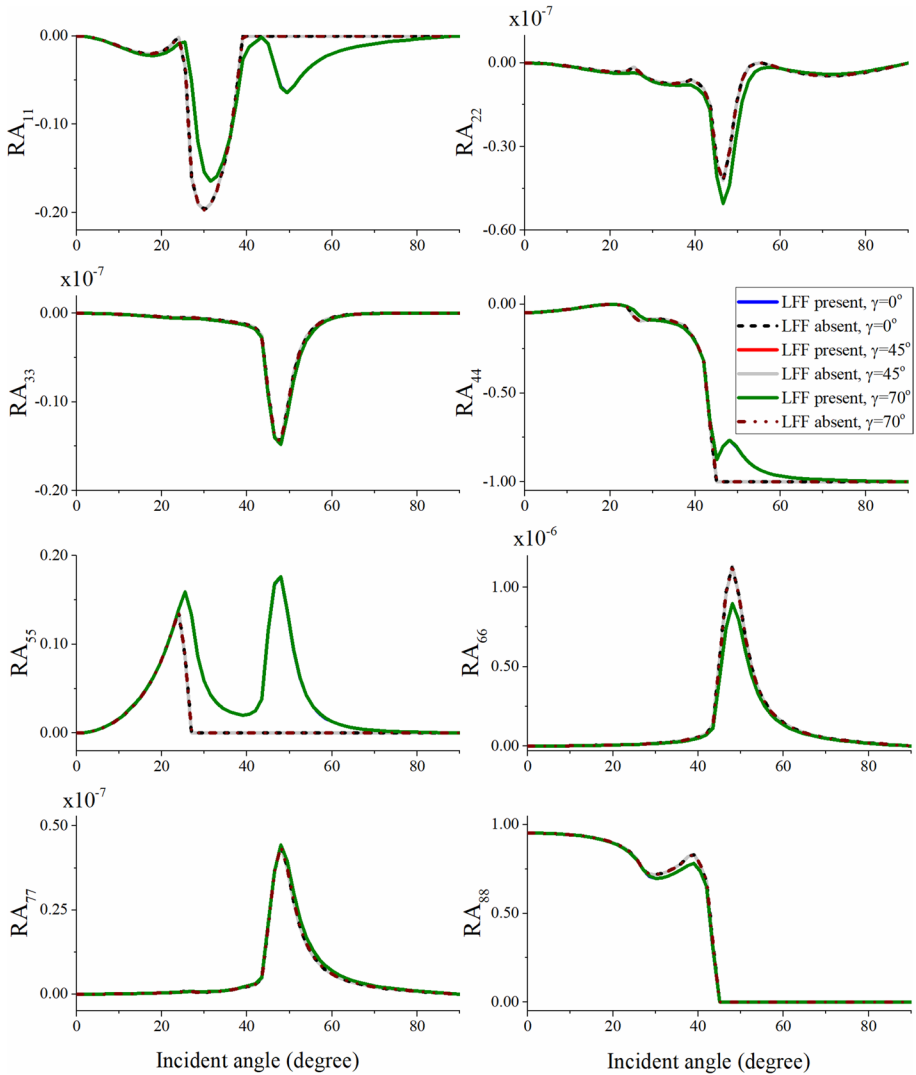
Fig. 16 Energy ratios as a function of the incidence angle at 42 Hz with different inhomogeneity angles, when the interface is sealed (incident SV wave). Irrespective of the LFF being absent or present, the corresponding three curves with different inhomogeneity angles overlap

# 7 Full-wave modeling and frequency-dependent AVO

In this section, numerical wavefield simulations are further carried out to validate the reflection and transmission behaviors. Moreover, the effect of frequency on the coefficients is studied, with application to amplitude versus offset (AVO).

7.1 Wave simulation in double-porosity media

Wang et al. (2019) developed a numerical algorithm for simulation of wave propagation in Biot–Rayleigh double-porosity media, including the LFF effect and its influence on the dispersion and attenuation of the P1 and SV waves. The algorithm also allows computing wavefields in the absence of LFF accurately. Without LFF, the velocity-stress equations for non-uniform porosity in the 2D case are given by Wang et al. (2019)

$$
\begin{aligned}
\dot{\sigma}_{xx} &= \lambda_c \big(\partial_x v_x + \partial_z v_z \big) + 2\mu \partial_x v_x + \alpha_1 M_1 \big(\partial_x q_x^{(1)} + \partial_z q_z^{(1)} \big) + \alpha_2 M_2 \big(\partial_x q_x^{(2)} + \partial_z q_z^{(2)} \big) \\
\dot{\sigma}_{zz} &= \lambda_c \big(\partial_x v_x + \partial_z v_z \big) + 2\mu \partial_z v_z + \alpha_1 M_1 \big(\partial_x q_x^{(1)} + \partial_z q_z^{(1)} \big) + \alpha_2 M_2 \big(\partial_x q_x^{(2)} + \partial_z q_z^{(2)} \big) \\
\dot{P}_{f1} &= -\alpha_1 M_1 \big(\partial_x v_x + \partial_z v_z \big) - M_1 \big(\partial_x q_x^{(1)} + \partial_z q_z^{(1)} \big) \\
\dot{P}_{f2} &= -\alpha_2 M_2 \big(\partial_x v_x + \partial_z v_z \big) - M_2 \big(\partial_x q_x^{(2)} + \partial_z q_z^{(2)} \big) \\
\dot{\sigma}_{xz} &= \mu \big(\partial_z v_x + \partial_x v_z \big),
\end{aligned}
\tag{48}
$$

Fig. 17 Snapshots of **a** the solid vertical particle velocity component v_z and **b** the energy, at 300 ms, corresponding to the double-porosity reflection-transmission problem, in the absence of local fluid flow (LFF)
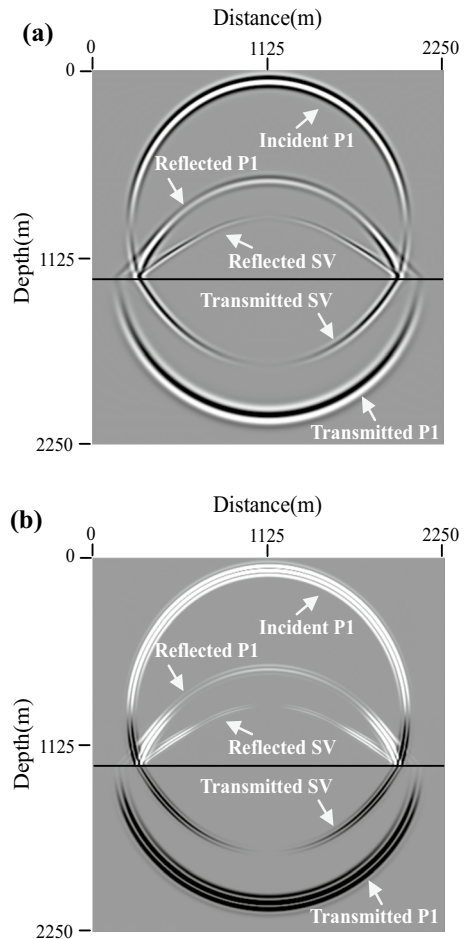
and

$$\begin{pmatrix} \rho & \rho_f & \rho_f \\ \rho_f & m_1 & 0 \\ \rho_f & 0 & m_2 \end{pmatrix} \begin{pmatrix} \dot{v}_i \\ \dot{q}_i^{(1)} \\ \dot{q}_i^{(2)} \end{pmatrix} = \begin{pmatrix} \partial_x \sigma_{ix} + \partial_z \sigma_{iz} \\ -\partial_i P_{f1} - b_1 q_i^{(1)} \big/ \left(\phi_1\right)^2 \\ -\partial_i P_{f2} - b_2 q_i^{(2)} \big/ \left(\phi_2\right)^2 \end{pmatrix}, \quad i = x, z, \tag{49}$$

where v_i, $q_i^{(1)}$, and $q_i^{(2)}$ are the solid and relative fluid particle velocity components determined by

$$v_i = \dot{u}_i, \ q_i^{(1)} = \phi_1\left(\dot{U}_i^{(1)} - \dot{u}_i\right), \ q_i^{(2)} = \phi_2\left(\dot{U}_i^{(2)} - \dot{u}_i\right), \ i = x, z. \tag{50}$$

The simulations based on Eqs. (48) and (49) are carried out with a grid method using staggered-grid Fourier differential operator and a second-order time-integration algorithm. The presence of slow quasi-static modes (the slow waves) in Eq. (49) makes the differential equations stiff and a time-splitting integration algorithm is used to solve the stiff part analytically (Wang et al. 2019). The numerical mesh has 451×451 points with a grid spacing of 5 m in both axes. The interface is located at a depth of 1250 m. The source, located at (1125, 950) m, is a Ricker-type wavelet with a dominate frequency of 42 Hz. It is implemented in the solid stress components (i.e., σ_{xx} and σ_{zz}) to generate incident P1-wave energy. Figure 17a shows a snapshot of the vertical solid particle velocity at 0.3 s, which covers the incidence angles from 0° to approximately 68°. Figure 17b displays the corresponding energy snapshot at 0.3 s. No slow compressional waves are observed due to the strong dissipation and attenuation. Some qualitative interpretation can be attempted from Fig. 17b. First, in agreement with RA_{55} in Fig. 6, most of the incident energy is transmitted as P1 wave when the incidence angle is small. The energy of transmitted P1 wave decreases with increasing incidence angle, in agreement with RA_{55}. Second, the energies of the reflected and transmitted SV waves are very low at normal incidence, as predicted by RA_{44} and RA_{88} in Fig. 6. With increasing incidence angle, the energy of the transmitted SV wave increases first and then decreases beyond approximately 50°, in agreement with RA_{88}. The energy of the reflected SV wave first increases, and after attaining a maximum, it decreases, and then sharply increases; this agrees with RA_{44}. Also in agreement is the energy variation of the reflected P1 wave. Its energy decreases firstly, attains a minimum, and then increases, as predicted by RA_{11} in Fig. 6. Evidently, the energy variations derived from the wave simulations exhibit similar trends as those predicted by Eq. (33), which indicates that the analysis is correct.

7.2 Frequency-Dependent AVO

In exploration geophysics, frequency-dependent reflection AVO has been widely discussed (Castagna et al. 1998; Liu et al. 2011; Zhao et al. 2015). Many factors affect AVO, with velocity dispersion being an important factor. The Biot–Rayleigh theory predicts comparable velocity dispersion as measured in rocks (Ba et al. 2011), and therefore, its transmission and transmission behaviors exhibit frequency-dependent characteristics.

Figure 18 shows the magnitudes and phases of the reflection and transmission coefficients of the P1 and SV waves as a function of frequency at three incidence angles (0°,
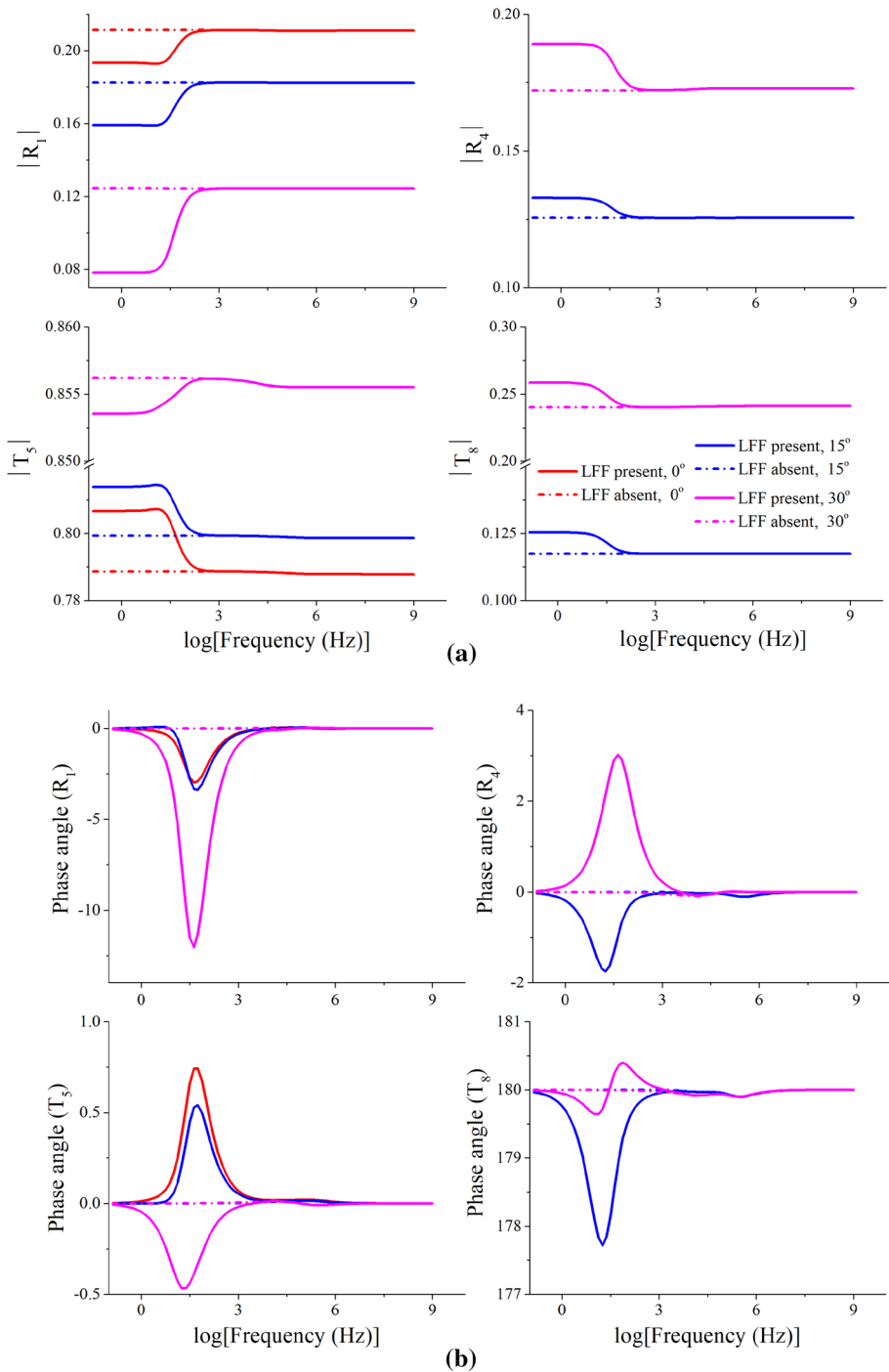
Fig. 18 Magnitudes (**a**) and phases (**b**) of the reflection and transmission coefficients of the P1 and SV waves as a function of frequency at three different incidence angles (incident P1 wave). The solid and dashed lines correspond to the presence and absence of LFF. The inhomogeneity angle is at 45°
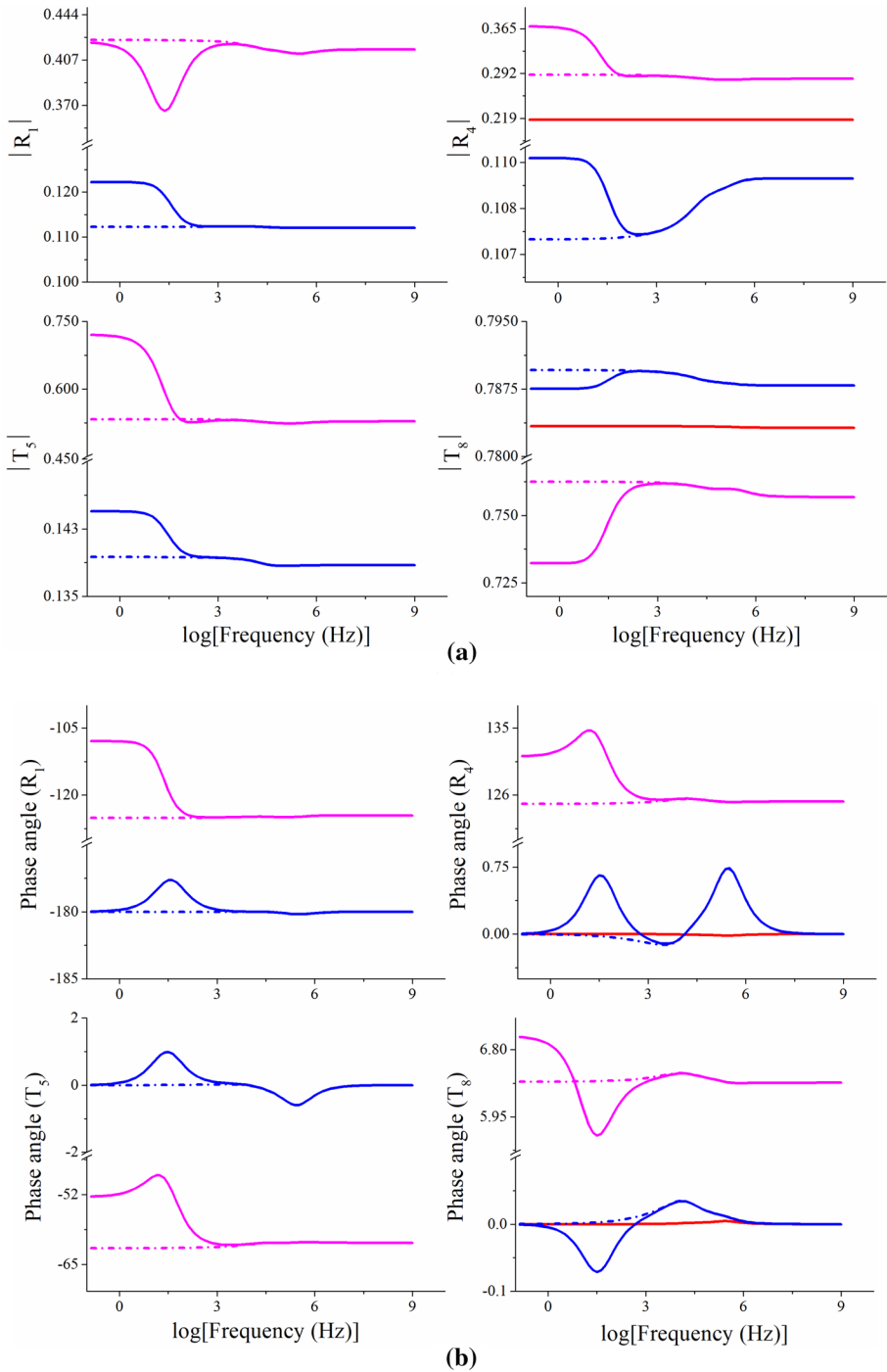
(a)

(b)

Fig. 19 Same as Fig. 18 but for incident SV wave

15°, and 30°), in the case of P1-wave incidence, irrespective of the interface being open or sealed, since they are not affected. At normal incidence, no shear wave occurs. In the presence of LFF, the magnitudes and phases of all the reflected and transmitted P1 and SV waves exhibit significant frequency-dependent characteristics from 20 to 200 Hz, corresponding to the exploration-geophysics frequency band. The maximum phase delay is approximately 12°. Zhao et al. (2015) obtained a similar dispersion trend for the P1 reflection coefficient at normal incidence, using the effective Biot theory obtained from the double-porosity theory of Pride et al. (2004). The frequency-dependent behavior illustrated here can be attributed to the frequency-dependent phase velocities displayed in Fig. 2. In contrast, the magnitudes and phases of the reflected and transmitted P1 and SV waves show no significant frequency dependence in the absence of LFF. For frequencies higher than 10 kHz, the LFF makes no difference to the P1 and SV reflection and transmission coefficients, and no evident frequency dependence can be appreciated.

Figure 19 shows the results for an incident SV wave. At normal incidence, no P1 wave occurs, and there exists no evident frequency dependence for the reflected and transmitted SV waves. For the other two incidence angles, noticeable frequency dependence can be appreciated in the presence of LFF, which mainly occurs between 10^{-1} and 10^3 Hz. The magnitudes and phase angles are affected and vary with frequency due to the LFF. In contrast, they do not change in the absence of LFF. The frequency-dependent behavior derived here provides insights for improving reservoir characterization.

8 Conclusions

We have computed the reflection and transmission coefficients of plane waves at an interface separating two double-porosity media for open and sealed boundary conditions. The waves are expressed in terms of potential functions specified by the propagation and attenuation directions, and the complex velocities. The aim is to study the influence of the local fluid flow (LFF) on wave propagation. Full-wave numerical simulations validate the results. The main conclusions are summarized as follows.

(1) The phase velocity of the P1 wave is more affected by frequency in the presence of the LFF effect, in comparison with the P2, P3, and SV waves. The model predicts the velocity dispersion level observed in rocks at the exploration-geophysics frequency band, and frequency-dependent reflection and transmission coefficients.

(2) For the case considered, the P1 wave is not attenuated if the LFF effect is absent. In this case, the transmitted P1 wave degenerates into a surface wave and there is not vertical energy flux beyond the critical angle. When the LFF effect is present, the medium behaves anelastically, and the transmitted P1 wave is not confined to the interface but propagates into the medium beyond the critical angle. The presence of the LFF effect results in more interference fluxes, irrespective of the interface being open or sealed. Meanwhile, we test the energy conservation at the interface.

(3) The inhomogeneity angle affects the reflection and transmission characteristics only when the LFF is present and the incidence is compressional.

(4) The reflection and transmission behaviors of the P1 and SV waves are not affected by the type of boundary condition, while those of the P2 and P3 waves are significantly affected, with the sealed boundary causing a significant decrease in magnitude and energy.

(5) The wavefield simulations corresponding to the reflection and transmission problem confirm the results of the plane-wave analysis.

The findings provide insights for improving reservoir characterization in typical fluid-saturated porous media.

Appendix 1

Let us denote the volume fractions of the two phases by v_1 and v_2 ($v_2 = 1 - v_1$), the two local porosities in the host and inclusions by ϕ_{10} and ϕ_{20}, the densities of solid grain and fluid by ρ_s and ρ_f, the grain bulk and shear moduli by K_s and μ_s, the fluid bulk modulus by K_f, the two kinds of permeability by κ_1 and κ_2, the fluid viscosity by η, the radius of the inclusion by R_0, and the three consolidation parameters by c_1, c_2 and c_s.

In uniform porosity case, the two partial porosities are defined by Ba et al. (2011)

$$\phi_1 = v_1 \phi_{10}, \phi_2 = v_2 \phi_{20}, \phi = \phi_1 + \phi_2, \tag{51}$$

where ϕ is the total porosity. The five density parameters in Eq. (1) are defined as

$$
\begin{aligned}
&\rho_{11} = (1 - \phi)\rho_s - (\phi - 1)\big/\big(2\rho_f\big) \\
&\rho_{22} = \big(\phi_1 + v_1\big)\rho_f\big/2, \ \rho_{33} = \big(\phi_2 + v_2\big)\rho_f\big/2 \\
&\rho_{12} = \big(\phi_1 - v_1\big)\rho_f\big/2, \ \rho_{13} = \big(\phi_2 - v_2\big)\rho_f\big/2.
\end{aligned}
\tag{52}
$$

The stiffness parameters are

$$
\begin{aligned}
&K_{b1} = \frac{(1 - \phi_{10})K_s}{1 + c_1 \phi_{10}}, K_{b2} = \frac{(1 - \phi_{20})K_s}{1 + c_2 \phi_{20}}, \mu_b = \frac{(1 - \phi)\mu_s}{1 + c_s \phi}, \\
&1\big/K_b = v_1\big/K_{b1} + v_2\big/K_{b2}, \\
&\beta = \frac{\phi_{20}\big[1 - (1 - \phi_{10})K_s\big/K_{b1}\big]}{\phi_{10}\big[1 - (1 - \phi_{20})K_s\big/K_{b2}\big]}, \gamma = \frac{K_s\big[\phi_2 + \beta\phi_1\big]}{K_f\big[1 - \phi - K_b\big/K_s\big]}, \\
&Q_1 = \frac{\beta\phi_1 K_s}{\beta + \gamma}, Q_2 = \frac{\phi_2 K_s}{1 + \gamma}, R_1 = \frac{\phi_1 K_f}{1 + \beta/\gamma}, R_2 = \frac{\phi_2 K_f}{1 + 1/\gamma}, \\
&A = (1 - \phi)K_s - 2\mu_b\big/3 - K_s\big(Q_1 + Q_2\big)\big/K_f, \ N = \mu_b.
\end{aligned}
\tag{53}
$$

b_1 and b_2 are

$$b_1 = \phi_1 \phi_{10} \eta\big/\kappa_1, b_2 = \phi_2 \phi_{20} \eta\big/\kappa_2. \tag{54}$$

In the non-uniform porosity case (Wang et al. 2019),

$$\alpha_1 = \phi_1 + \frac{\beta\phi_1 K_s}{\gamma K_f}, \alpha_2 = \phi_2 + \frac{\phi_2 K_s}{\gamma K_f}, M_1 = \frac{K_f}{\phi_1(1 + \beta/\gamma)}, M_2 = \frac{K_f}{\phi_2(1 + 1/\gamma)}. \quad (55)$$

Parameter λ_c is

$$\lambda_c = -\frac{2}{3}\mu + (1 - \phi)K_s$$
$$+ \left(1 - K_s/K_f\right)\left(\alpha_1 M_1 \phi_1 + \alpha_2 M_2 \phi_2 - M_1 \phi_1^2 - M_2 \phi_2^2\right) + \left(\alpha_1 M_1 \phi_1 + \alpha_2 M_2 \phi_2\right). \quad (56)$$

Following Eqs. (55) and (53), the relations among Q_i, R_i, α_i, and M_i are

$$Q_i = \phi_i M_i (\alpha_i - \phi_i), R_i = \phi_i^2 M_i, \quad i = 1, 2. \quad (57)$$

The density ρ is

$$\rho = (1 - \phi)\rho_s + \phi\rho_f. \quad (58)$$

Appendix 2

The elements of matrix G in Eq. (33) are

$$G_{1l} = s_z^l, \ (l = 1, 2, 3), \quad G_{14} = s_x^4, \quad G_{1l} = -s_z^l, \ (l = 5, 6, 7), \quad G_{18} = -s_x^8. \quad (59)$$

$$G_{2l} = s_x^l, \ (l = 1, 2, 3), \quad G_{24} = -s_z^4, \quad G_{2l} = -s_x^l, \ (l = 5, 6, 7), \quad G_{28} = s_z^8. \quad (60)$$

$$G_{3l} = \left(D_1^{\mathrm{I}} + D_2^{\mathrm{I}}\delta_{f1s}^l + D_3^{\mathrm{I}}\delta_{f2s}^l\right)\left(\left(s_x^l\right)^2 + \left(s_z^l\right)^2\right) - 2\mu^{\mathrm{I}}\left(s_z^l\right)^2, (l = 1, 2, 3)$$
$$G_{34} = -2\mu^{\mathrm{I}}s_x^4 s_z^4$$
$$G_{3l} = -\left[\left(D_1^{\mathrm{II}} + D_2^{\mathrm{II}}\delta_{f1s}^l + D_3^{\mathrm{II}}\delta_{f2s}^l\right)\left(\left(s_x^l\right)^2 + \left(s_z^l\right)^2\right) - 2\mu^{\mathrm{II}}\left(s_z^l\right)^2\right], (l = 5, 6, 7) \quad (61)$$
$$G_{38} = 2\mu^{\mathrm{II}}s_x^8 s_z^8.$$

$$G_{4l} = 2\mu^{\mathrm{I}}s_x^l s_z^l, (l = 1, 2, 3), G_{44} = \mu^{\mathrm{I}}\left(\left(s_x^4\right)^2 - \left(s_z^4\right)^2\right)$$
$$G_{4l} = -2\mu^{\mathrm{II}}s_x^l s_z^l, (l = 5, 6, 7), G_{48} = -\mu^{\mathrm{II}}\left(\left(s_x^8\right)^2 - \left(s_z^8\right)^2\right). \quad (62)$$

For the open boundary,

$$G_{5l} = \phi_1^{\mathrm{I}}\left(\delta_{f1s}^l - 1\right)s_z^l, (l = 1, 2, 3), G_{54} = \phi_1^{\mathrm{I}}\left(\delta_{f1s}^4 - 1\right)s_x^4$$
$$G_{5l} = -\phi_1^{\mathrm{II}}\left(\delta_{f1s}^l - 1\right)s_z^l, (l = 5, 6, 7), G_{58} = -\phi_1^{\mathrm{II}}\left(\delta_{f1s}^8 - 1\right)s_x^8. \quad (63)$$

$$G_{6l} = \left(D_4^{\mathrm{I}} + D_5^{\mathrm{I}}\delta_{f1s}^l + D_6^{\mathrm{I}}\delta_{f2s}^l\right)\left(\left(s_x^l\right)^2 + \left(s_z^l\right)^2\right), (l = 1, 2, 3), G_{64} = 0$$
$$G_{6l} = -\left[\left(D_4^{\mathrm{II}} + D_5^{\mathrm{II}}\delta_{f1s}^l + D_6^{\mathrm{II}}\delta_{f2s}^l\right)\left(\left(s_x^l\right)^2 + \left(s_z^l\right)^2\right)\right], (l = 5, 6, 7), G_{68} = 0. \quad (64)$$

$$G_{7l} = \phi_2^{\mathrm{I}}\left(\delta_{f2s}^l - 1\right)s_z^l, (l = 1, 2, 3), G_{74} = \phi_2^{\mathrm{I}}\left(\delta_{f2s}^4 - 1\right)s_x^4$$

$$G_{7l} = -\phi_2^{\mathrm{II}}\left(\delta_{f2s}^l - 1\right)s_z^l, (l = 5, 6, 7), G_{78} = -\phi_2^{\mathrm{II}}\left(\delta_{f2s}^8 - 1\right)s_x^8. \tag{65}$$

$$G_{8l} = \left(D_7^{\mathrm{I}} + D_8^{\mathrm{I}}\delta_{f1s}^l + D_9^{\mathrm{I}}\delta_{f2s}^l\right)\left(\left(s_x^l\right)^2 + \left(s_z^l\right)^2\right), (l = 1, 2, 3), G_{84} = 0$$

$$G_{8l} = -\left[\left(D_7^{\mathrm{II}} + D_8^{\mathrm{II}}\delta_{f1s}^l + D_9^{\mathrm{II}}\delta_{f2s}^l\right)\left(\left(s_x^l\right)^2 + \left(s_z^l\right)^2\right)\right], (l = 5, 6, 7), G_{88} = 0. \tag{66}$$

For the sealed boundary,

$$G_{5l} = \phi_1^{\mathrm{I}}\left(\delta_{f1s}^l - 1\right)s_z^l, (l = 1, 2, 3), G_{54} = \phi_1^{\mathrm{I}}\left(\delta_{f1s}^4 - 1\right)s_x^4$$

$$G_{5l} = 0, (l = 5, 6, 7), G_{58} = 0. \tag{67}$$

$$G_{6l} = 0, (l = 1, 2, 3), G_{64} = 0$$

$$G_{6l} = -\phi_1^{\mathrm{II}}\left(\delta_{f1s}^l - 1\right)s_z^l, (l = 5, 6, 7), G_{68} = -\phi_1^{\mathrm{II}}\left(\delta_{f1s}^8 - 1\right)s_x^8. \tag{68}$$

$$G_{7l} = \phi_2^{\mathrm{I}}\left(\delta_{f2s}^l - 1\right)s_z^l, (l = 1, 2, 3), G_{74} = \phi_2^{\mathrm{I}}\left(\delta_{f2s}^4 - 1\right)s_x^4$$

$$G_{7l} = 0, (l = 5, 6, 7), G_{78} = 0. \tag{69}$$

$$G_{8l} = 0, (l = 1, 2, 3), G_{84} = 0$$

$$G_{8l} = -\phi_2^{\mathrm{II}}\left(\delta_{f2s}^l - 1\right)s_z^l, (l = 5, 6, 7), G_{88} = -\phi_2^{\mathrm{II}}\left(\delta_{f2s}^8 - 1\right)s_x^8. \tag{70}$$

In the case of an incident P1 wave, irrespective of the boundary being open or sealed, the first four elements in y are

$$y_1 = -s_z^0, y_2 = -s_x^0,$$

$$y_3 = -\left[\left(D_1^{\mathrm{I}} + D_2^{\mathrm{I}}\delta_{f1s}^0 + D_3^{\mathrm{I}}\delta_{f2s}^0\right)\left(\left(s_x^0\right)^2 + \left(s_z^0\right)^2\right) - 2\mu^{\mathrm{I}}\left(s_z^0\right)^2\right], y_4 = -2\mu^{\mathrm{I}}s_x^0 s_z^0 \tag{71}$$

For the open boundary,

$$y_5 = -\phi_1^{\mathrm{I}}\left(\delta_{f1s}^0 - 1\right)s_z^0, y_6 = -\left[\left(D_4^{\mathrm{I}} + D_5^{\mathrm{I}}\delta_{f1s}^0 + D_6^{\mathrm{I}}\delta_{f2s}^0\right)\left(\left(s_x^0\right)^2 + \left(s_z^0\right)^2\right)\right],$$

$$y_7 = -\phi_2^{\mathrm{I}}\left(\delta_{f2s}^0 - 1\right)s_z^0, y_8 = -\left[\left(D_7^{\mathrm{I}} + D_8^{\mathrm{I}}\delta_{f1s}^0 + D_9^{\mathrm{I}}\delta_{f2s}^0\right)\left(\left(s_x^0\right)^2 + \left(s_z^0\right)^2\right)\right]. \tag{72}$$

For the sealed boundary,

$$y_5 = -\phi_1^{\mathrm{I}}\left(\delta_{f1s}^0 - 1\right)s_z^0, y_6 = 0, y_7 = -\phi_2^{\mathrm{I}}\left(\delta_{f2s}^0 - 1\right)s_z^0, y_8 = 0. \tag{73}$$

In the case of an incident SV wave, irrespective of the boundary being open or sealed, the elements in *y* are

$$y_1 = -s_x^0, \; y_2 = s_z^0, \; y_3 = 2\mu^{\mathrm{I}} s_x^0 s_z^0, \; y_4 = -\mu^{\mathrm{I}}\left(\left(s_x^0\right)^2 - \left(s_z^0\right)^2\right). \tag{74}$$

$$y_5 = -\phi_1^{\mathrm{I}}\left(\delta_{f1s}^0 - 1\right)s_x^0, \; y_6 = 0, \; y_7 = -\phi_2^{\mathrm{I}}\left(\delta_{f2s}^0 - 1\right)s_x^0, \; y_8 = 0. \tag{75}$$

The parameters D_i^{I} and D_i^{II} in Eqs. (61), (64), (66), (71), and (72) are given in "Appendix 3".

Appendix 3

The expressions for $D_i^{\mathrm{I}}(i = 1, 2, \ldots, 8, 9)$ in Eq. (38) in medium Ω_1 are

$$
\begin{aligned}
D_1^{\mathrm{I}} = &-\lambda_c^{\mathrm{I}} + \alpha_1^{\mathrm{I}} M_1^{\mathrm{I}} \phi_1^{\mathrm{I}} + \alpha_2^{\mathrm{I}} M_2^{\mathrm{I}} \phi_2^{\mathrm{I}} \\
&+ \frac{3\phi_{10}^{\mathrm{I}}}{F^{\mathrm{I}}} \phi_1^{\mathrm{I}} \phi_2^{\mathrm{I}} \left(\alpha_1^{\mathrm{I}} M_1^{\mathrm{I}} - \alpha_2^{\mathrm{I}} M_2^{\mathrm{I}}\right)\left(\alpha_1^{\mathrm{I}} M_1^{\mathrm{I}} - \alpha_2^{\mathrm{I}} M_2^{\mathrm{I}} + M_2^{\mathrm{I}} \phi_2^{\mathrm{I}} - M_1^{\mathrm{I}} \phi_1^{\mathrm{I}}\right),
\end{aligned}
\tag{76}
$$

$$D_2^{\mathrm{I}} = -\alpha_1^{\mathrm{I}} M_1^{\mathrm{I}} \phi_1^{\mathrm{I}} + \frac{3\phi_{10}^{\mathrm{I}}}{F^{\mathrm{I}}} \phi_1^{\mathrm{I}} \phi_2^{\mathrm{I}} \left(\alpha_1^{\mathrm{I}} M_1^{\mathrm{I}} - \alpha_2^{\mathrm{I}} M_2^{\mathrm{I}}\right) M_1^{\mathrm{I}} \phi_1^{\mathrm{I}}, \tag{77}$$

$$D_3^{\mathrm{I}} = -\alpha_2^{\mathrm{I}} M_2^{\mathrm{I}} \phi_2^{\mathrm{I}} - \frac{3\phi_{10}^{\mathrm{I}}}{F^{\mathrm{I}}} \phi_1^{\mathrm{I}} \phi_2^{\mathrm{I}} \left(\alpha_1^{\mathrm{I}} M_1^{\mathrm{I}} - \alpha_2^{\mathrm{I}} M_2^{\mathrm{I}}\right) M_2^{\mathrm{I}} \phi_2^{\mathrm{I}}, \tag{78}$$

$$D_4^{\mathrm{I}} = \alpha_1^{\mathrm{I}} M_1^{\mathrm{I}} - M_1^{\mathrm{I}} \phi_1^{\mathrm{I}} - \frac{3\phi_{10}^{\mathrm{I}}}{F^{\mathrm{I}}} M_1^{\mathrm{I}} \phi_1^{\mathrm{I}} \phi_2^{\mathrm{I}} \left(\alpha_1^{\mathrm{I}} M_1^{\mathrm{I}} - \alpha_2^{\mathrm{I}} M_2^{\mathrm{I}} + M_2^{\mathrm{I}} \phi_2^{\mathrm{I}} - M_1^{\mathrm{I}} \phi_1^{\mathrm{I}}\right), \tag{79}$$

$$D_5^{\mathrm{I}} = M_1^{\mathrm{I}} \phi_1^{\mathrm{I}} - \frac{3\phi_{10}^{\mathrm{I}}}{F^{\mathrm{I}}} M_1^{\mathrm{I}} \phi_1^{\mathrm{I}} \phi_2^{\mathrm{I}} M_1^{\mathrm{I}} \phi_1^{\mathrm{I}}, \tag{80}$$

$$D_6^{\mathrm{I}} = \frac{3\phi_{10}^{\mathrm{I}}}{F^{\mathrm{I}}} M_1^{\mathrm{I}} \phi_1^{\mathrm{I}} \phi_2^{\mathrm{I}} M_2^{\mathrm{I}} \phi_2^{\mathrm{I}}, \tag{81}$$

$$D_7^{\mathrm{I}} = \alpha_2^{\mathrm{I}} M_2^{\mathrm{I}} - M_2^{\mathrm{I}} \phi_2^{\mathrm{I}} + \frac{3\phi_{10}^{\mathrm{I}}}{F^{\mathrm{I}}} M_2^{\mathrm{I}} \phi_1^{\mathrm{I}} \phi_2^{\mathrm{I}} \left(\alpha_1^{\mathrm{I}} M_1^{\mathrm{I}} - \alpha_2^{\mathrm{I}} M_2^{\mathrm{I}} + M_2^{\mathrm{I}} \phi_2^{\mathrm{I}} - M_1^{\mathrm{I}} \phi_1^{\mathrm{I}}\right), \tag{82}$$

$$D_8^{\mathrm{I}} = \frac{3\phi_{10}^{\mathrm{I}}}{F^{\mathrm{I}}} M_2^{\mathrm{I}} \phi_1^{\mathrm{I}} \phi_2^{\mathrm{I}} M_1^{\mathrm{I}} \phi_1^{\mathrm{I}}, \tag{83}$$

$$D_9^{\mathrm{I}} = M_2^{\mathrm{I}} \phi_2^{\mathrm{I}} - \frac{3\phi_{10}^{\mathrm{I}}}{F^{\mathrm{I}}} M_2^{\mathrm{I}} \phi_1^{\mathrm{I}} \phi_2^{\mathrm{I}} M_2^{\mathrm{I}} \phi_2^{\mathrm{I}}, \tag{84}$$

where

$$F^{\mathrm{I}} = \phi_{20}^{\mathrm{I}} \left(R_0^{\mathrm{I}}\right)^2 \rho_f^{\mathrm{I}} \phi_1^{\mathrm{I}} \omega^2 - i\omega \phi_{20}^{\mathrm{I}} \left(R_0^{\mathrm{I}}\right)^2 \frac{\phi_{10}^{\mathrm{I}} \phi_1^{\mathrm{I}} \eta_1^{\mathrm{I}}}{\kappa_1^{\mathrm{I}}} + 3\phi_{10}^{\mathrm{I}} \phi_1^{\mathrm{I}} \phi_2^{\mathrm{I}} \left(M_1^{\mathrm{I}} + M_2^{\mathrm{I}}\right). \tag{85}$$

By replacing index I with II in Eqs. (76)–(85), the corresponding formulae for medium Ω_2 can be obtained.

References

Agersborg R, Johansen TA, Jakobsen M (2009) Velocity variations in carbonate rocks due to dual porosity and wave-induced fluid flow. Geophys Prospect 57(1):81–98

Arora A, Tomar SK (2008) The effect of inertial coupling on seismic reflection amplitudes. Geophys Prospect 56(5):643–654

Arora A, Painuly A, Tomar SK (2015) Body waves in composite solid matrix containing two immiscible fluids. Transp Porous Med 108(3):531–554

Ba J, Carcione JM, Nie J (2011) Biot–Rayleigh theory of wave propagation in double-porosity media. J Geophys Res Solid Earth 116:B06202

Berryman JG, Wang HF (2000) Elastic wave propagation and attenuation in a double-porosity dual-permeability medium. Int J Rock Mech Min 37(1–2):63–78

Biot MA (1956) Theory of propagation of elastic waves in a fluid-saturated porous solid. I. Low frequency range. J. Acoust. Soc. Am. 28(2):168–178

Biot MA (1962) Mechanics of deformation and acoustic propagation in porous media. J Appl Phys 33(4):1482–1498

Borcherdt RD (1982) Reflection–refraction of general P-and type-I S-waves in elastic and anelastic solids. Geophys J Int 70(3):621–638

Brajanovski M, Müller TM, Gurevich B (2006) Characteristic frequencies of seismic attenuation due to wave-induced fluid flow in fractured porous media. Geophys J Int 166(2):574–578

Brutsaert W (1964) The propagation of elastic waves in unconsolidated unsaturated granular mediums. J Geophys Res 69(2):243–257

Carcione JM (2014) Wave fields in real media. Theory and numerical simulation of wave propagation in anisotropic, anelastic, porous and electromagnetic media, 3rd edn. Elsevier, Amsterdam

Carcione JM, Picotti S (2006) P-wave seismic attenuation by slow wave diffusion. Effects of inhomogeneous rock properties. Geophysics 71(3):O1–O8

Carcione JM, Seriani G (2001) Wave simulation in frozen porous media. J Comput Phys 170:676–695

Carcione JM, Tinivella U (2000) Bottom-simulating reflectors: seismic velocities and AVO effect. Geophysics 65(1):54–67

Carcione JM, Morency C, Santos JE (2010) Computational poroelasticity: a review. Geophysics 75:A229–A243

Castagna JP, Swan HW, Foster DJ (1998) Framework for AVO gradient and intercept interpretation. Geophysics 63(3):948–956

Cui ZW, Wang KX (2003) Influence of the squirt flow on reflection and refraction of elastic waves at a fluid/fluid-saturated poroelastic solid interface. Int J Eng Sci 41(18):2179–2191

Dai Z, Kuang Z, Zhao S (2006a) Reflection and transmission of elastic waves from the interface of a fluid-saturated porous solid and a double porosity solid. Transp Porous Med 65(2):237–264

Dai Z, Kuang Z, Zhao S (2006b) Reflection and transmission of elastic waves at the interface between an elastic solid and a double porosity medium. Int J Rock Mech Min 6(43):961–971

Denneman AIM, Drijkoningen GG, Smeulders DMJ, Wapenaar K (2002) Reflection and transmission of waves at a fluid/porous-medium interface. Geophysics 67(1):282–291

Deresiewicz H, Rice JT (1962) The effect of boundaries on wave propagation in a liquid-filled porous solid: III. Reflection of plane waves at a free plane boundary (general case). Bull Seismol Soc Am 52(3):595–625

Deresiewicz H, Rice JT (1964) The effect of boundaries on wave propagation in a liquid-filled porous solid-V: transmission across plane interface. Bull Seismol Soc Am 54(1):409–416

Dutta NC, Odé H (1983) Seismic reflections from a gas–water contact. Geophysics 48(2):148–162

Gurevich B, Zyriano VB, Lopatnikov SL (1997) Seismic attenuation in finely layered porous rocks: effects of fluid flow and scattering. Geophysics 62(1):319–324

Gurevich B, Ciz R, Denneman AIM (2004) Simple expressions for normal incidence reflection coefficients from an interface between fluid-saturated porous materials. Geophysics 69(6):1372–1377

Kumar M, Saini R (2012) Reflection and refraction of attenuated waves at boundary of elastic solid and porous solid saturated with two immiscible viscous fluids. Appl Math Mech Engl 33(6):797–816

Kumar M, Sharma MD (2013) Reflection and transmission of attenuated waves at the boundary between two dissimilar poroelastic solids saturated with two immiscible viscous fluids. Geophys Prospect 61(5):1035–1055

Leclaire P, Cohen-Ténoudji F, Aguirre-Puente J (1994) Extension of Biot's theory of wave propagation to frozen porous media. J Acoust Soc Am 96(6):3753–3768

Liu L, Cao S, Wang L (2011) Poroelastic analysis of frequency-dependent amplitude-versus-offset variations. Geophysics 76(3):C31–C40

Lo WC, Sposito G, Majer E (2005) Wave propagation through elastic porous media containing two immiscible fluids. Water Resour Res 41(2):W02025

Müller TM, Gurevich B, Lebedev M (2010) Seismic wave attenuation and dispersion resulting from wave-induced flow in porous rocks—a review. Geophysics 75(5):75A147–75A164

Painuly A, Arora A (2018) Reflection and transmission of inhomogeneous waves in a composite porous solid saturated by two immiscible fluids. Geophys Prospect 66(1):182–196

Pride SR, Berryman JG (2003a) Linear dynamics of double porosity dual-permeability materials. I. Governing equations and acoustic attenuation. Phys Rev E 68(3):036603

Pride SR, Berryman JG (2003b) Linear dynamics of double porosity dual-permeability materials. II. Fluid transport equations. Phys Rev E 68(3):036604

Pride SR, Berryman JG, Harris JM (2004) Seismic attenuation due to wave-induced flow. J Geophys Res 109:B01201

Rubino JG, Ravazzoli CL, Santos JE (2006) Reflection and transmission of waves in composite porous media: a quantification of energy conversions involving slow waves. J Acoust Soc Am 120(5):2425–2436

Santos JE, Douglas J Jr, Corbero J, Lovera OMA (1990) A model for wave propagation in a porous medium saturated by a two phase fluid. J Acoust Soc Am 87(4):1439–1448

Santos JE, Corbero JM, Ravazzoli CL, Hensley JL (1992) Reflection and transmission coefficients in fluid-saturated porous media. J Acoust Soc Am 91(4):1911–1923

Santos JE, Ravazzoli CL, Carcione JM (2004) A model for wave propagation in a composite solid matrix saturated by a single-phase fluid. J Acoust Soc Am 115(6):2749–2760

Sharma MD (2013) Effect of local fluid flow on reflection of plane elastic waves at the boundary of a double-porosity medium. Adv Water Resour 61:62–73

Sharma MD, Kumar M (2011) Reflection of attenuated waves at the surface of a porous solid saturated with two immiscible viscous fluids. Geophys J Int 184(1):371–384

Shekhar S, Parvez IA (2016) Reflection and refraction of attenuated waves at the interface between cracked poroelastic medium and porous solid saturated with two immiscible fluids. Transp Porous Med 113(2):405–430

Sidler R, Carcione JM, Holliger K (2013) A pseudospectral method for the simulation of 3-D ultrasonic and seismic waves in heterogeneous poroelastic borehole environments. Geophys J Int 196:1134–1151

Tomar SK, Arora A (2006) Reflection and transmission of elastic waves at an elastic/porous solid saturated by two immiscible fluids. Int J Solids Struct 43(7–8):1991–2013

Tuncay K, Corapcioglu MY (1997) Wave propagation in poroelastic media saturated by two fluids. J Appl Mech 64(2):313–320

Wang E, Carcione JM, Ba J (2019) Wave simulation in double-porosity media based on the Biot–Rayleigh theory. Geophysics 84:WA11–WA21

Yeh CL, Lo WC, Jan CD, Yang CC (2010) Reflection and refraction of obliquely incident elastic waves upon the interface between two porous elastic half-spaces saturated by different fluid mixtures. J Hydrol 395(1–2):91–102

Zhao L, Han DH, Yao Q, Zhou R, Yan F (2015) Seismic reflection dispersion due to wave-induced fluid flow in heterogeneous reservoir rocks. Geophysics 80(3):D221–D235